Cloud Property Retrievals Using ATSR-2

Christopher Peter Arnold

Supervised by: Dr R. G. Grainger

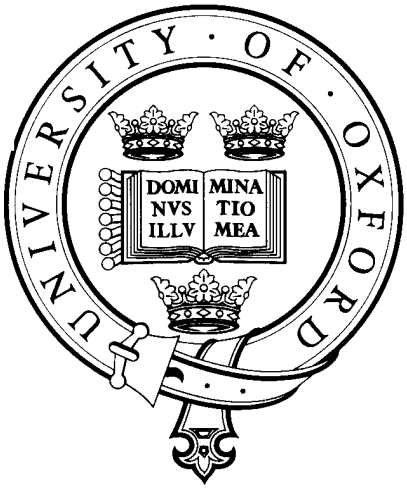

Transfer of Status Report
Trinity Term 2009

Atmospheric, Oceanic and Planetary Physics
Department of Physics
University of Oxford

Acknowledgements

I am very grateful to Andrew Sayer and to Don Grainger for the support and guidance they have given me over the past year and for their comments on this report. It is a pleasure to be a member of a very active research group and I have come to truly appreciate the support of my colleagues both in Oxford and at the Rutherford Appleton Laboratory. I feel very fortunate to have been awarded a NERC studentship and I hope that the work described in this report reflects my enthusiasm and effort.

Christopher Arnold — August 2009, Oxford

Contents

List of Figures

List of Tables

Chapter 1

Clouds: formation, classification and influence

Figure 1: An example of an orographic ‘cap cloud’ over Mount Fiji.
[Source: http://pixdaus.com/pics/4ESnHSUQyi8g.jpg]

1.1 Cloud formation

Clouds form when the relative humidity of a ‘parcel’ of atmospheric air exceeds some critical point. The relative humidity (f) of an air ‘parcel’ at a fixed pressure p and temperature T is given by:

$$f(p,T) = \frac{w}{w_{\mathrm{s}}(p,T)} \tag{1}$$

where w is the mass mixing ratio of water in the parcel and w_{s} is the mass mixing ratio of water in a saturated parcel. When $w > w_{\mathrm{s}}$ the air is said to be ‘supersaturated’ and cloud formation can take place. The prevalent mechanism for creating supersaturated air parcels is cooling, due to the strong temperature dependence of w_{s}. In the atmosphere, air parcels are cooled by conduction, thermal emission and the adiabatic expansion of ascending air (lifting). Four principal cloud formation mechanisms can be identified:

- **Large-scale frontal lifting of air** occurs when large bodies of air of different densities come into contact. This process tends to form **stratiform clouds** that are very uniform over a wide spatial extent.

- **Thermally-driven updrafts** occur when the surface of the Earth is warmed by the sun, in turn warming the atmosphere directly above it. A thermal updraft is created, causing air to rise and then cool adiabatically. Clouds formed in this way are known as **convective clouds**.

- **Orographically forced lifting** occurs when air is forced to rise as it is driven over surface relief by the wind. An example of an **orographic cloud** is the 'cap cloud' shown in figure 1.

- **Radiative cooling** occurs when the atmosphere is cooled due to its thermal emission. This is most likely to happen during the night. Fog is formed in this way.

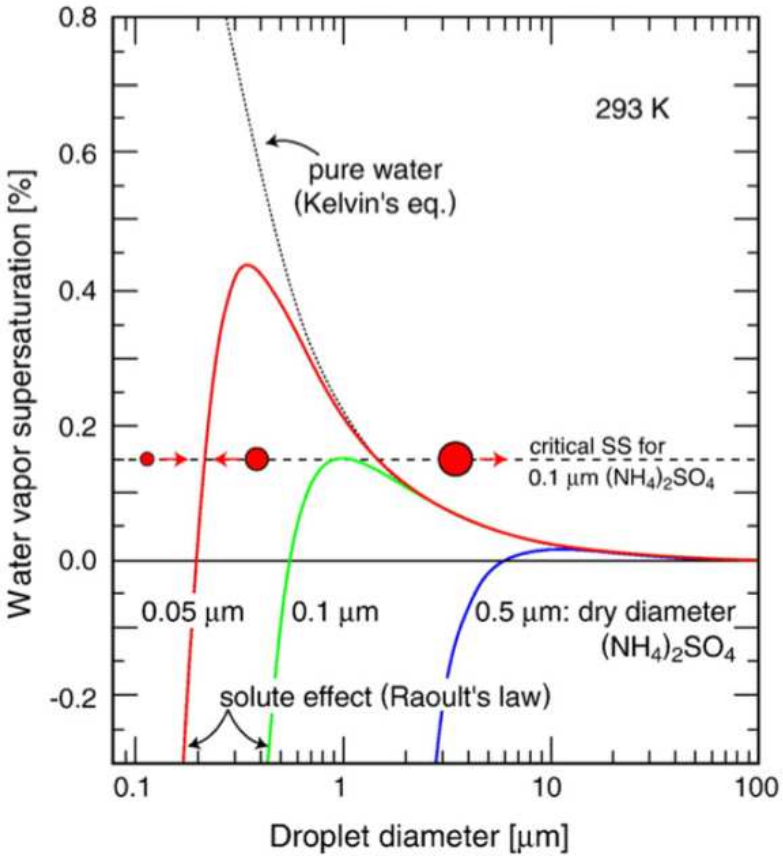

Figure 2

Microphysics of droplet formation When air is 'supersaturated', water condenses onto small particles in the atmosphere called cloud condensation nuclei [CCN], to form small droplets ($\lesssim 0.5\ \mu$m

in diameter). For a cloud to form, the rate at which water condenses onto these droplets must exceed the rate at which it evaporates from their surface. This is not generally the case; evaporation and condensation tend to remain in stable equilibrium and the droplets do not grow. Cloud droplets develop when the supersaturation of water in the atmosphere reaches a critical level, at which this equilibrium breaks down. According to Köhler theory [Köhler, 1936], this critical level is dependent on the particular type of CCN particle and its diameter.

Figure 2 shows examples of 'Köhler curves' for ammonium sulphate crystals of three different sizes. The peak of each curve corresponds to the level of supersaturation required for that particular CCN particle to become 'activated'. When a CCN particle is 'activated', the droplet is able to grow for as long as the air in the surrounding atmosphere remains supersaturated.

Cloud condensation nuclei CCN can range from soot and dust particles to marine organic molecules and sea salt; they tend to have a relatively short lifetime in the atmosphere and are most likely to be found in high concentrations at low altitudes. The ability of a particle to act as a CCN chiefly depends on its size and soluble mass fraction.

1.2 Classifying clouds

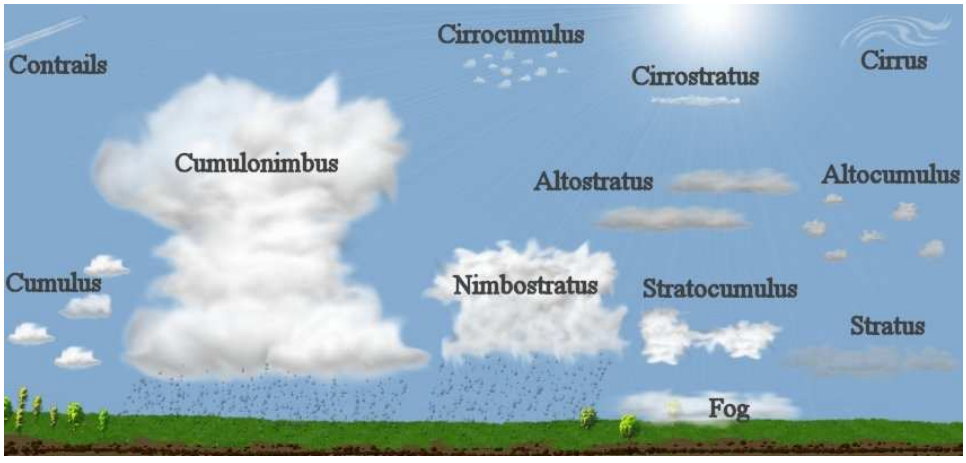

Figure 3: A pictorial representation of the major cloud types.
[Source: http://www.terrapsych.com/cloud_ classifications.jpg]

There are 10 major cloud types, as shown pictorially in figure 3. These cloud types can be split into three main groups based on their typical altitude range (see table 1). In general, different cloud

types are formed by the different 'lifting' processes outlined in section 1.1 and are seeded by different CCN particles.

Height range	Cloud type	Base height (km)	Base temperature (K)	Cloud thickness (m)	Particle phase
High	Cirrus (Ci)	5–15	200–240	500–2000	ice
	Cirrostratus (Cs)	5–15	230–245	1000–2000	ice
	Cirrocumulus (Cc)	5–15	230–245	100–300	water/mixed
Medium	Altostratus (As)	3–8	240–260	1000–3000	ice/mixed
	Altocumulus (Ac)	2–8	240–280	100–1000	water/mixed
	Nimbostratus (Ns)	0.5–2	260–280	2000–10000	ice/mixed
Low	Cumulonimbus (Cb)	1–4	270–300	2000–20000	mixed
	Cumulus (Cu)	1–4	270–300	500–4000	water
	Stratocumulus (Sc)	0–2	265–295	100–2000	water/mixed
	Stratus (St)	0–2	265–295	100–500	water

Table 1: The properties of the 10 principal cloud types.

1.3 The influence of cloud on our climate

Clouds interact with the Earth's climate system through a wide variety of complex feedback processes, however it is possible to split this interaction into two broad mechanisms:

- **Transport of heat and moisture.** When clouds form, a large amount of latent heat energy is released into the atmosphere. This release of latent heat high in the atmosphere has the net effect of reducing the tropospheric lapse rate from the 'dry' value of 9.8 K km^{-1} to a value of the order of 6–7 K km^{-1}. Since clouds are principally responsible for maintaining the lapse rate, they play a key role in coupling the effect of any radiative forcing at the tropopause to the surface. Clouds thus effect the degree to which changes in the radiation budget at the tropopause affect the atmospheric conditions and temperature at the surface.

- **Moderating the planetary radiation budget.** Clouds scatter and reflect incident solar radiation back towards space. Upwelling infrared radiation from the atmosphere is absorbed by clouds and re-emitted in all directions. As a result, clouds tend to have a net cooling effect on the planet during the day and a warming effect during the night. Higher clouds are more likely to warm the planet, since they 'trap' a larger amount of infrared radiation than low clouds (because there is a deeper atmospheric column below the cloud). The exact radiative 'footprint' of

a cloud however depends on a combination of its macrophysical and microphysical properties; different types of clouds have different effects on the Earth's radiation budget.

Cloud radiative forcing The cloud radiative forcing, C, is a useful measure of the impact of clouds on the planetary radiation budget. In order to define C, it is necessary to consider a cloudy 'domain', incorporating regions of clear sky and overcast regions. In this cloudy 'domain', the net radiative heating over the entire atmospheric column is given by:

$$H = S(1 - \alpha) - F \tag{2}$$

where S is the solar irradiance and α is the albedo. The cloud radiative forcing is defined as the difference between the net column-integrated radiative heating in the region, H, and the heating that would occur in the same region if no clouds were present, H_{clear}.

$$C = H - H_{\text{clear}} \tag{3}$$

The cloud radiative forcing can be separated into a short-wave [SW] and a long-wave [LW] component:

$$C = C_{\text{SW}} + C_{\text{LW}} \tag{4}$$

where $C_{\text{SW}} = S(\alpha_{\text{clear}} - \alpha)$ and $C_{\text{LW}} = F_{\text{clear}} - F$.

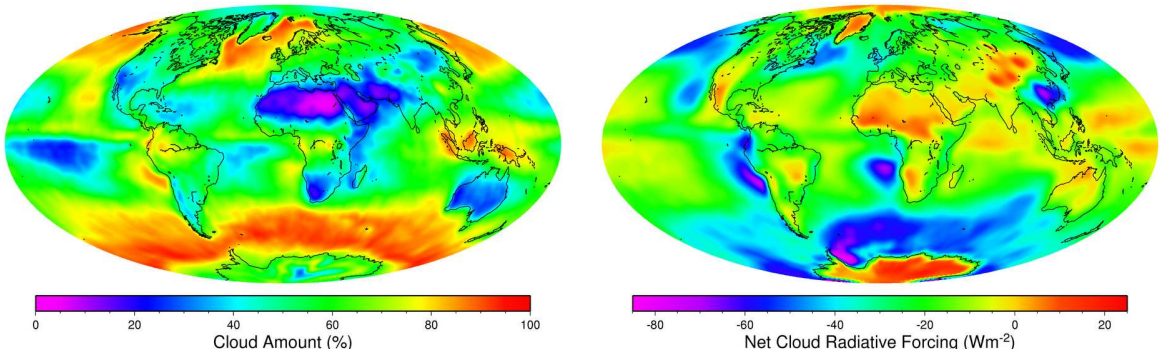

(a) Annual mean cloud amount (b) Annual mean cloud radiative forcing

Figure 4: Annual mean cloud fraction and net cloud radiative forcing, as derived by the MODIS and CERES instruments aboard the NASA satellite Terra.
[Source: http://science.larc.nasa.gov/ceres/press_ releases/]

The cloud radiative forcings, C_{SW} and C_{LW} have been monitored by the 'Earth Radiation Budget Experiment' [ERBE] [Barkstrom et al., 1990] and, more recently, the 'Clouds and the Earth's Radiant Energy System' [CERES] experiment [Wielicki et al., 1996]. Figure 4(a) shows the annual mean (March 2000 to February 2001) net cloud radiative forcing measured by the CERES instrument aboard the NASA satellite Terra. Figure 4(a) shows the mean cloud amount for the same period, as observed by the MODIS instrument [Minnis et al., 2003] also aboard Terra. The global mean net cloud radiative forcing is ≈ 48 W m^{-2}. Clouds are an integral element of the Earth's climate system and perturbations to the cloud radiative forcing have the potential to play a key role in future climate change.

According to the latest IPCC report, the role of cloud feedback processes in climate models represents the greatest source of uncertainty in predictions of the impact of rises in greenhouse gas concentrations [Intergovernmental Panel on Climate Change, 2007].

1.4 Anthropogenic effects on the cloud system

1.4.1 Cloud indirect effects

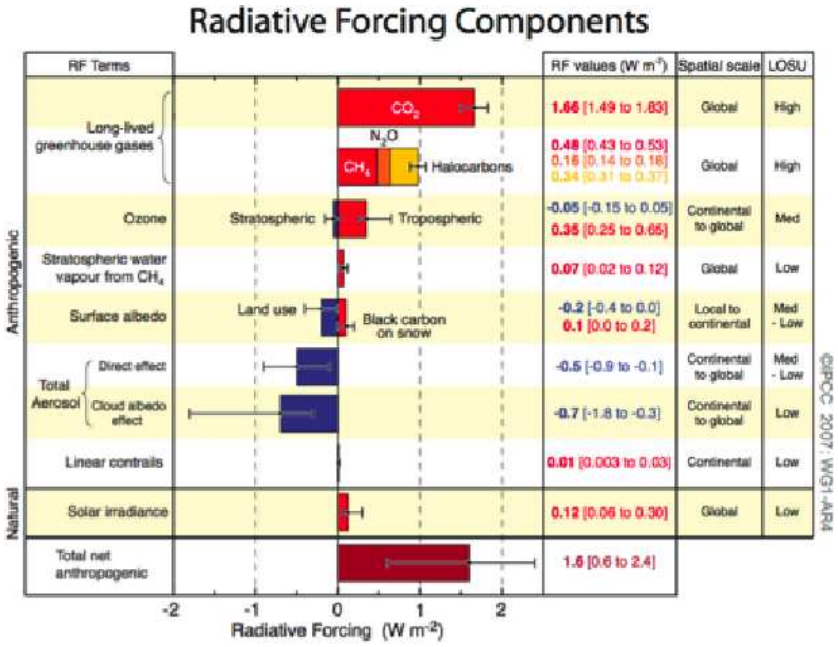

Figure 5: A plot showing the principal changes in radiative forcing originating from anthropogenic activity between 1750 and 2005. The error bars denote the range of uncertainty in each component of the net forcing. From: Intergovernmental Panel on Climate Change [2007].

When a cloud forms in a region of high aerosol loading, a large number of CCN are available to 'seed' cloud droplets. If a fixed atmospheric water content is assumed, this results in the formation of a larger number of droplets in the cloud, each of a smaller mean size and in turn increases the cloud albedo [Twomey, 1997]. This effect is referred to as the 'first indirect effect' or the 'cloud albedo effect' and corresponds to a net negative radiative forcing at the tropopause. A clear illustration of the effect is given by the bright tracks observed in decks of marine stratocumulus where the cloud has been contaminated by aerosol from ship exhausts, known as 'ship tracks' [Campmany et al., 2009]. Although the effect has been observed in a number of studies [Bréon et al., 2002; Bulgin et al., 2008; Koren et al., 2005], it is still poorly quantified in model simulations of climate change [Quaas et al., 2008]: figure 5 shows a plot from the latest IPCC report [Solomon et al., 2007] which identifies the cloud albedo as the most uncertain component in the net anthropogenic radiative forcing.

In addition, aerosols can suppress precipitation and increase cloud lifetimes through 'secondary indirect effects' [Rosenfeld, 1999, 2000; Ackerman et al., 2000]. These effects are referred to as 'cloud lifetime effects' and again result in a negative radiative forcing. These effects were not taken into account in the latest IPCC report, since their level of scientific understanding [LOSU] was considered to be too low. Lohmann and Feichter [2005] however report the current best estimate of the radiative forcing due to the cloud lifetime effect to be -0.85 ± 0.55. It is clear that in order to understand climate change, it is vital to understand the effect of aerosols on clouds at a global scale. The development of accurate cloud climatologies from satellite data is an important step in achieving this goal.

Chapter 2

The ATSR-2 instrument

2.1 The ATSR missions

The Along Track Scanning Radiometer [ATSR] instruments were originally designed to make accurate measurements of Sea Surface Temperature [SST] [Delderfield et al., 1986; Edwards et al., 1990]. The unique viewing geometry of the instruments allows near-simultaneous measurements to be made of the Earth's surface through two atmospheric paths of differing lengths. Thus, it is possible to discriminate the contribution to each measurement arising from the atmosphere and the surface[1]. In addition, a reduction can be made in the retrieval noise, since any systematic errors in measurements from both views can be made to cancel.

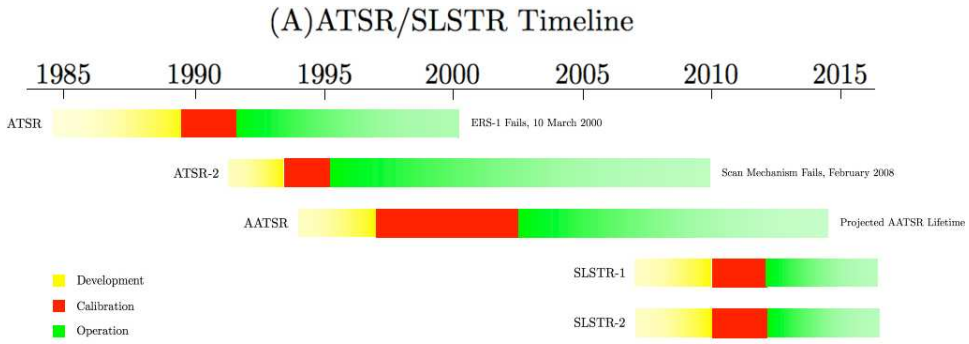

Figure 6: Time series of the (A)ATSR/SLSTR instruments.

The ATSR instruments are carefully calibrated both before and during operation, as described in section 2.6. As a result, the combined data set now comprises more than 17 years of consistent measurements. The dates of launch and operation of the ATSR instruments are summarised in figure 6. The figure also includes the Sea and Land Surface Temperature Radiometer [SLSTR] instruments, which are scheduled to fly on the Meteosat satellites Sentinel-3A and Sentinel-3B in 2012[2].

[1] Only 'clear' scenes are used for SST measurements; pixels containing cloud or optically thick aerosol are rejected.
[2] Please consult Nieke et al. [2008] for more details of the SLSTR missions, which are currently under development.

2.2 ATSR-2

The second Along-Track Scanning Radiometer instrument [ATSR-2] flies aboard the European Research Satellite ERS-2, which was launched in April 1995. The instrument makes radiance measurements at the top of the atmosphere [TOA] in seven spectral channels: four in the visible [VIS] and near-infrared [NIR] and three in the thermal infrared [IR]. The VIS/NIR channels, which are required to perform cloud retrievals, were not present on ATSR-1.

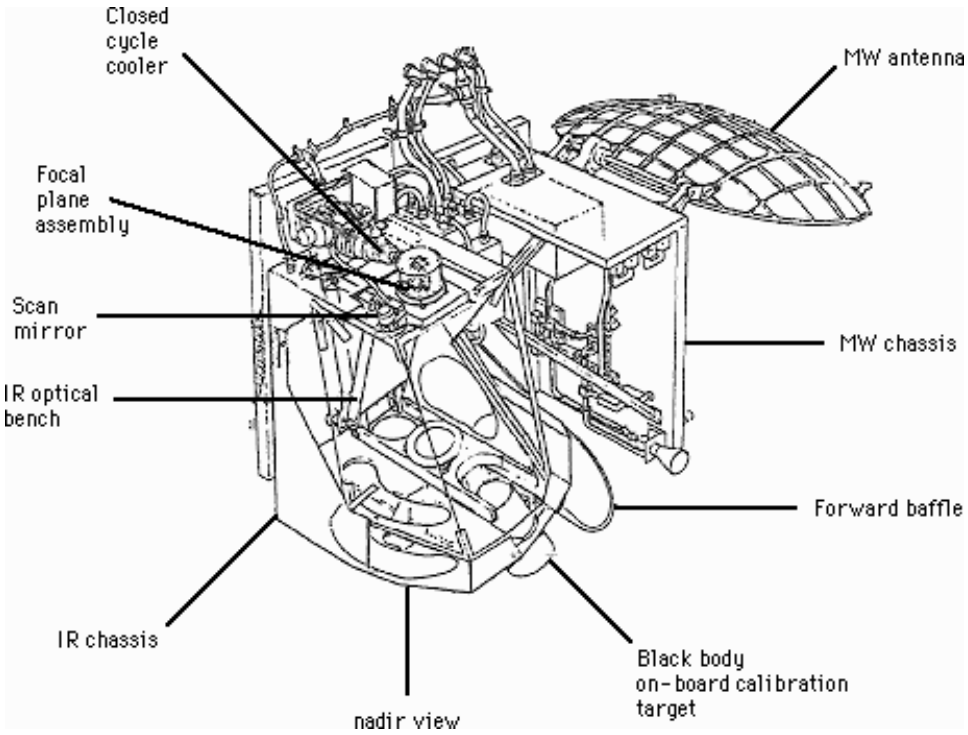

Figure 7: ATSR-2 instrument structure. Taken from: Llewllyn-Jones et al. [2001].

2.3 The satellite platform

ERS-2 is in a sun-synchronous polar orbit at a mean altitude of 785 km, with an inclination of 98.5° to the equator. The mean local solar time [MLST] for the descending node is 10.30 am at the equator. The satellite takes 100 minutes to orbit the earth and its orbit cycle repeats once every 35 days. Consecutive orbits are separated by a distance of 80 km at the equator. The orbit is carefully controlled to ensure that it remains within a maximum deviation of ± 1 km on the ground and ± 5 minutes on the MLST at the equator. As well as ATSR-2, the ERS-2 payload includes the Global Ozone Monitoring Experiment [GOME] instrument, a Radar Altimeter [RA], a Microwave Radiometer [MWR] and a

Wind Scatterometer [WS] [Francis et al., 1995].

2.4 Instrument design

The design of ATSR-2 is shown in figure 7. Radiance measurements are made in seven wavelength channels, viewing at both near-nadir and along the track. The channels used are displayed in table 2. ATSR-2 has a signal to noise [S:N] ratio of 20:1 at 0.5% spectral albedo and noise equivalent temperatures [NEΔTs] of less than $\pm$ 0.05 K in all channels. Before launch, the 11 μm and 12 μm channels were characterised by NEΔTs at 270 K of 21 mK and 25 mK respectively [Mutlow et al., 1999].

Channel	Bandwidth
0.55 μm	20 nm
0.67 μm	20 nm
0.87 μm	20 nm
1.6 μm	0.3 μm
3.7 μm	0.3 μm
10.8 μm	1.0 μm
12.0 μm	1.0 μm

Table 2: The ATSR-2 channels: location and bandwidth.

Radiation enters the ATSR-2 instrument through two arc-shaped windows, which are baffled to ensure that the field of view [FOV] is not contaminated by direct sunlight. The incoming radiation is directed by the rotating scan mirror onto a paraboloid mirror, from where it is reflected and focussed into the visible and infrared focal plane assemblies [FPAs]. The FPAs are maintained at temperatures of 256K and 80K respectively, in order to minimise noise. At the FPAs, the radiance measured in each channel is converted to an electronic signal which can be transmitted down to the earth. The ERS-2 satellite suffers from bandwidth limitations and as a result the swath width is reduced by a factor of 2 over the ocean.

The viewing geometry of the ATSR instruments is shown in figure 8. During a single scan, the region sampled corresponds to two elliptical arcs on the surface of the Earth, each approximately 500 km wide. In the nadir view, which contains 555 pixels, the satellite zenith angle ranges between 0° and 22°. In the forward view, containing 371 pixels, this range is between 53° and 55°. The satellite moves 1 km forward during each scan cycle, corresponding to a central pixel size of 1$\times$1 km

in the nadir view and 1.5×2 km in the forward view. The scan cycle repeats 6.6 times per second. Given a mean instrument altitude of 785 km, the central forward view pixel lies approximately 1000 km in front of the corresponding nadir pixel at any moment in time. The nadir and forward view measurements of a single 'point' on the Earth's surface will therefore be separated by $\sim$150 seconds, which is shorter than the timescale of typical atmospheric processes. As a result, the two views can be treated as 'simultaneous'; providing two different measurements of *the same* scene.

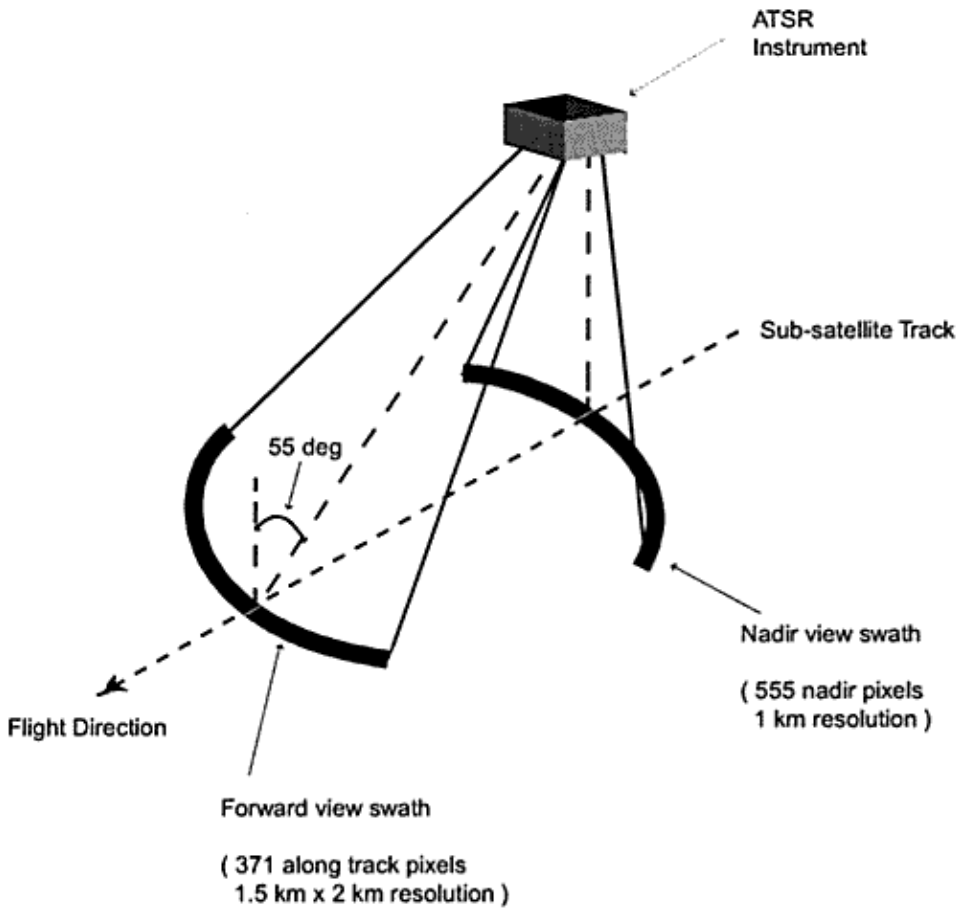

Figure 8: The (A)ATSR viewing geometry, taken from Mutlow et al. [1999]

2.5 ATSR-2 Data

The ATSR-2 data used in the Oxford University and Rutherford Appleton Laboratory ATSR Cloud Retrieval [ORAC-ATSR] is in the form of an 'ungridded brightness temperature/reflectance' [UBT] product. The data is stored in exactly the same way as it is accumulated by the instrument, on a scan by scan basis. A 'line' of pixels in the product record corresponds to a curved swath of pixels of varying sizes on the Earth's surface. Radiance measurements in the ATSR-2 visible channels

are stored as a 12-bit count (thus taking a value between 0 and 4095), which must be converted to a 'sun-normalised reflectance' before being ingested into the ORAC-ATSR retrieval code. This is done using calibration tables, which are produced using information from the visible calibration system [VISCAL] on board ATSR-2 [Mutlow et al., 1999]. The ground coordinates of each pixel are also stored in the UBT files, along with quality control information and a cloud mask.

2.6 Instrument calibration

The calibration of the ASTR-2 instrument is well documented by Mutlow et al. [1999] and Smith et al. [1997]. A brief summary of the post-launch calibration is presented below.

IR channels As shown in figure 9, ATSR-2 images two calibration black-body targets during each scan cycle. These are maintained at 265K and 305K respectively, which lie near the limits of the range of brightness temperatures typically observed by the instrument [Mason et al., 1996]. The blackbodies are monitored continuously to ensure that their temperatures remain constant. Approximately once each year, a 'blackbody crossover test' is performed in which both blackbodies are allowed to reach the same ambient temperature and their radiometric signals are compared [Smith, 2008].

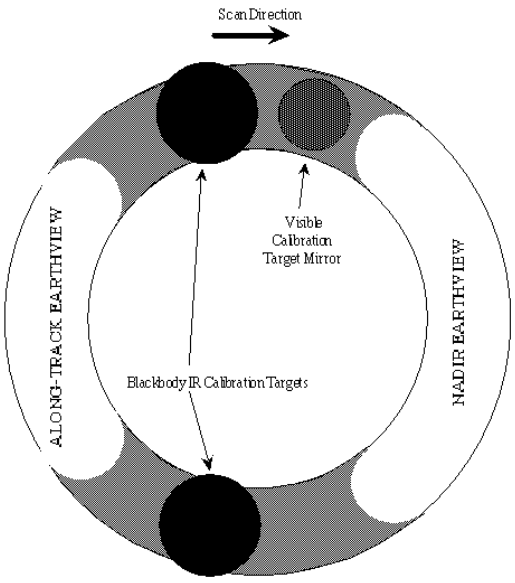

Figure 9: The (A)ATSR scan cycle, taken from Llewllyn-Jones et al. [2001].

Visible channels The ATSR-2 visible calibration system [VISCAL] is described thoroughly by Smith et al. [1997]. At one point in each orbit, when the sun is at normal incidence[3], sunlight is admitted to the instrument through a UV filter and reflected onto the FPAs using an opal mirror. The VISCAL provides a radiance equivalent to a 25% signal from a Lambertian scatterer, which is used as the 'upper' measurement for the visible calibration. A zero radiance signal, obtained from the cooler of the onboard blackbodies, is used as the 'lower' measurement.

The harsh conditions of space tend to degrade the ATSR-2 VIS/NIR detectors. In addition, the cooled optical surfaces of the ATSR-2 instrument are prone to a gradual build-up of condensation, which can cause short-term fluctuations in the measured signal. It is therefore vital to monitor the performance of the entire VISCAL system vicariously. This is done by analysing measurements made of stable sites on the Earth's surface for which the bidirectional reflectance distribution function [BRDF] is well known [Smith, 1997; Smith et al., 2002].

2.7 ATSR-2 performance

The performance of the ATSR-2 instrument over its lifetime is reported by Mutlow et al. [2000] and Smith et al. [2002]. In general, the instrument has been able to fulfil its original specification, although interruptions to the data record have been caused by problems with the scan mechanism, as well as routine outgassing.

2.7.1 Outgassing

Several times each year, for a period of approximately two days at a time, the FPA is warmed up in order to vaporise any contaminants that have built up on its surface [Mutlow et al., 1999]. During this time no measurements can be made in the IR channels. Errors in the visible calibration are also likely, due to the rapid change in the throughput of the visible channels. This 'outgassing' process also contributes to the degradation of the FPAs.

[3] Sunlight is admitted to the instrument when a baffled tube which forms the 'inlet' of the VISCAL system is pointing directly at the sun.

2.7.2 Problems with the scan mechanism

ATSR-2 was taken out of operation between December 1995 and July 1996 due to a problem with its scanning mechanism. The instrument was re-started and has generally performed well ever since, although occasional 'jitters' in the scan mechanism have persisted. According to Mutlow et al. [1999], these 'jitters' are manifested as slipped lines of data in $\sim 1\%$ of forward view scenes. At present, forward view measurements are not used in the operational version of the ORAC-ATSR retrieval.

2.8 The AATSR instrument

Although the cloud retrieval algorithm described in this report was designed for ATSR-2 data, it can readily be applied to data from the Advanced Along Track Scanning Radiometer [AATSR], currently flying aboard the ESA satellite Envisat. AATSR is almost identical in operation to ATSR-2, but it does not suffer from the same data-downlinking limitations. For a complete description of the AATSR instrument please consult Llewllyn-Jones et al. [2001].

2.9 Other cloud retrieval algorithms using ATSR-2 data

Apart from the scheme described here, two major cloud retrieval schemes exist for ATSR-2 data. The first, developed at University College London, uses a stereo-matching algorithm to retrieve cloud fraction and cloud top height [Muller et al., 2007; Denis et al., 2007]. The scheme is analogous to a scheme that has been applied to the MISR instrument (see below) and the technique has been validated extensively [Naud et al., 2007]. The second technique, developed by González et al. [2002] is specifically designed to detect optical and microphysical parameters of cirrus clouds overlying a layer of water cloud. It uses a radiative transfer model to generate look up tables [LUTs] of predicted TOA radiance measurements in the 0.87 μm, 1.6 μm and 3.7 μm channels, which are then inverted using an evolutionary scatter search technique.

2.10 Other cloud measurement instruments

2.10.1 Satellite-borne instruments

AVHRR The Advanced Very High Resolution Radiometer [AVHRR] instruments have flown aboard the US National Oceanic and Atmospheric Administration [NOAA] polar-orbiting satellites since NOAA-6 (launched in 1979), as well as the TIROS-N (launched in 1978) and MetOp-A (launched in 2006) satellites [Kidwell, 2009]. Apart from the very first AVHRR (which flew aboard TIROS-N), the instruments make nadir radiance measurements in at least 5 channels in the visible and infrared. AVHRR has a resolution of $\sim$1 km at the nadir point. Cloud algorithms have been developed for the instrument at NOAA [Stowe et al., 2002; Jacobowitz et al., 2003] and the Royal Netherlands Meteorological Institute [KNMI] [Roebeling et al., 2003], as part of the 'satellite application facility on climate monitoring' [CM-SAF] [Woick et al., 2002]. These algorithms have been used to create cloud climatologies that span more than three decades. The AVHRR instruments do not have an on-board calibration system and there is some debate about the reliability of any long term trends observed in AVHRR data [Thomas et al., 2009]. Although there is evidence of a drift in calibration between the AVHRR instruments, many efforts have been made to improve the dataset using vicarious calibration methods, such as the monitoring of stable sites on the Earth's surface or of deep convective cloud systems [Rao and Chen, 1996; Doelling et al., 2004; Ignatov et al., 2005].

CALIOP The Cloud-Aerosol Lidar with Orthogonal Polarisation [CALIOP] flies aboard the Cloud Aerosol Lidar and Infrared Pathfinder Satellite Observation [CALIPSO] platform, which flies as part of the National Aeronautics and Space Administration [NASA] 'A Train' formation [Winker et al., 2004, 2006]. The instrument measures backscattered light intensity at 532 nm and 1064 nm, thus producing high resolution vertical profiles of clouds directly below the CALIPSO track, which are collocated with and near simultaneous to cloud observations from other A-Train instruments. CALIPSO also carries a Imaging Infrared Radiometer [IIR] which is used to detect the emissivity and effective radius of cirrus clouds, taking measurements at 8.7 μm, 10.5 μm and 12 μm [Winker et al., 2006]. The IIR has a swath width of 64 km, centred on the CALIOP track, and a resolution of 1×1 km. An example of cloud data derived from the CALIOP instrument is given in figure 10.

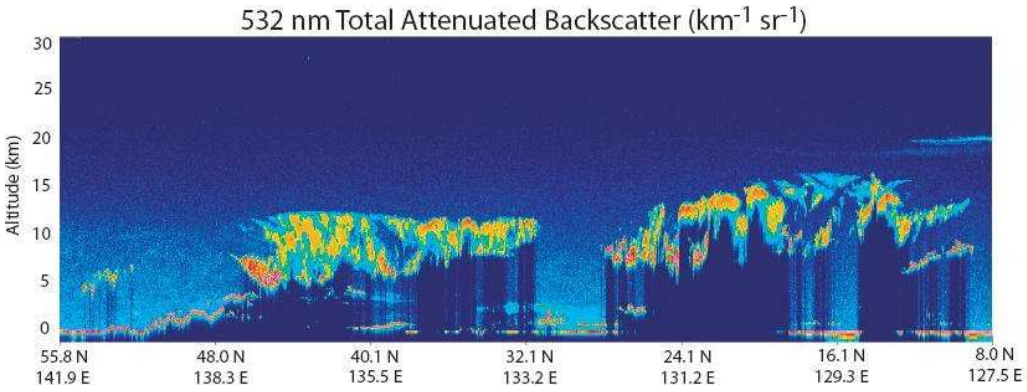

Figure 10: Total attenuated backscatter at 532 nm, as observed by the CALIOP instrument. [Source: www.alg.umbc.edu/usag/images/calipso1.jpg]

CPR The Cloud Profiling Radar [CPR] is a 94 GHz nadir viewing radar aboard the NASA satellite CloudSat, which flies as part of the A-Train [Stephens et al., 2002]. The instrument has a vertical resolution of 500 m, an along-track resolution of 1.7 km and an across-track resolution of 1.4 km. The instrument is primarily used for cloud detection, to make accurate measurements of cloud top height and to retrieve cloud effective radii.

MERIS The Medium Resolution Imaging Spectrometer [MERIS] flies alongside AATSR on the ESA platform Envisat, imaging the Earth in 15 visible channels with a resolution of $\sim 300 \times 300$ m [Louet, 2001]. MERIS is predominantly used to make measurements of ocean colour, however a cloud screening and aerosol retrieval algorithm that employs a synergy of data from the MERIS and AATSR instruments is currently under development [North et al., 2008]. Cloud algorithms using a synergy of AATSR and MERIS data are likely to be developed in the near future.

MIPAS The Michelson Interferometer for Passive Atmospheric Sounding [MIPAS] is a Fourier Transorm [FT] spectrometer that also flies aboard Envisat [Fischer et al., 2007; Louet, 2001]. Although MIPAS is predominantly used for Ozone and trace gas retrievals, a cloud retrieval scheme for the instrument has recently been developed at Oxford University [Hurley et al., 2009]. Although the horizontal resolution is poor, MIPAS is sensitive to thin cirrus clouds high in the atmosphere, which nadir viewing instruments often fail to detect.

MISR The Multi-angle Imaging Spectroradiometer [MISR] images the Earth in 4 channels in the visible and IR at a wide range of different viewing angles (nadir, $\pm 26.1°$, $\pm 45.6°$, $\pm 60.0°$, $\pm 70.5°$)

Figure 11: A MERIS image of the southern coast of Bangladesh.
[Source: www.seos-project.edu/modules/world-of-images/images/bangladesh_ meris.jpg]

[Diner et al., 1998]. The principal purpose of MISR is to provide information on how the surface, aerosols and clouds influence the planetary radiation budget, by making measurements of the scattered sunlight at different angles. The multiple viewing angles of the MISR instrument have also been harnessed by using stereo-matching techniques to retrieve cloud top height [Moroney et al., 2002]. Examples of the MISR cloud fraction products are given in section 4.1.

MODIS The Moderate Resolution Imaging Spectroradiometer [MODIS] flies aboard the NASA satellites Terra and Aqua [Salomonson et al., 2002, 1989]. Terra, launched in 2000 as part of the 'A-Train', has a MLST of 10:30 am for the descending node at the equator, while Aqua, launched in 2002, has a MLST at the equator of 13:30 pm for the ascending node. MODIS has a 55° swath width and thus global coverage can be achieved every $\sim$2 days. The instrument makes TOA radiance measurements at 36 bands in the visible and near-infrared, at a resolution of at least 1×1 km. Many cloud climatologies have been developed using MODIS data, but the most widely used are those of Platnick et al. [2003] and Minnis et al. [2003]. The extensive coverage of the MODIS instrument and the ability to gain information on the diurnal cycle of clouds using both Aqua and Terra data have

made MODIS data a widely used resource. MODIS is also used to provide surface information; the MODIS bidirectional surface reflectance [BRDF] product [Wanner et al., 1997] is used as a constraint in the cloud retrieval described in this report.

SCIAMACHY The Scanning Imaging Spectrometer for Atmospheric Chartography [SCIAMACHY] is the succesor to the GOME instrument that flies alongside ATSR-2 on ERS-2. SCIAMACHY flies aboard Envisat and makes measurements of the solar radiation that is transmitted, reflected and backscattered by the atmosphere [Louet, 2001; Bovensmann et al., 1999]. SCIAMACHY measurements are made over a range from 240 nm to 1700 nm and in selected bands between 2000 nm and 2400 nm, at a resolution of between 0.2 nm and 0.5 nm [Burrows et al., 1995]. A cloud retrieval has been developed for SCIAMACHY at the University of Bremen [Kokhanovsky et al., 2005], products from which have been compared with the cloud climatology described in this report [Rozanov et al., 2006].

SEVIRI The Spinning Enhanced Visible and Infra-Red Imager [SEVIRI] is an instrument aboard the European Organisation for the Exploitation of Meteorological Satellites [EUMETSAT] platforms Meteosat-8 and MeteoSat-9. SEVIRI images the Earth in 12 channels, 8 in the thermal IR with a resolution of 3×3 km and 4 in the visible with a resolution of up to 1×1 km [Aminou, 2002]. A number of SEVIRI cloud retrievals exist, which allows a range of retrieval methods to be compared using the same data [Thoss, 2008]. The Optimal Cloud Analysis [OCA] retrieval [Watts et al., 1998] developed for SEVIRI was used as the basis for the development of the ORAC-ATSR cloud retrieval algorithm described in this report. Thus, the intercomparison of OCA retrievals with other SEVIRI retrievals can yield insights into the operation of the ORAC-ATSR algorithm.

2.10.2 ISCCP

The International Satellite Cloud Climatology Project [ISSCP], which was established in 1982, uses data collected from a number of weather satellites to generate a climatology of cloud properties and cloud-type distributions [Rossow and Schiffer, 1991]. A particular focus is to study the diurnal, seasonal and interannual variations in the distribution of clouds and their properties [Rossow and Schiffer, 1999]. Although the ISCCP dataset extends from June 1983 to the present it is not

necessarily regarded as a reliable source of information on *trends* in cloud properties [Evan et al., 2007].

2.10.3 In-situ instruments

CFARR The Chilbolton Facility for Atmospheric and Radio Research[4] [CFARR], is a ground-based remote sensing facility in Hampshire, UK. A number of instruments used for cloud remote sensing are operational at the site[5], including a cloud camera, three radar instruments (3 GHz, 35 GHz and 94 GHz) and a lidar ceilometer [Wrench, 2009]. The lidar instrument measures the attenuated backscattered coefficient at 905 nm, and can thus be used to retrieve cloud base heights and cloud optical properties. The 3 GHz Chilbolton Advanced Meteorological Radar [CAMRa], has a dual-polarisation capacity and can therefore measure the size and orientation of cloud particles, as well as detecting atmospheric wind fields using Doppler methods [Goddard, 1995].

ARM The Atmospheric Radiation Measurement [ARM] program[6] [Stokes and Schwartz, 1994] operates a number of field sites, mobile facilities and aerial facilities for monitoring the atmosphere. An array of instruments similar to those at Chilbolton are installed at each site and a wide variety of cloud data is routinely produced.

FAAM The Facility for Airborne Atmospheric Measurements [FAAM] is an aircraft used to undertake a wide variety of atmospheric science studies. Campaigns are frequently undertaken over CFARR or collocated with satellite data to allow the intercomparison and validation of different data sets. Recent cloud campaigns undertaken using the FAAM aircraft include the Met Office RAIN-CLOUDS study, the VOCALS experiment and the CONSTRAIN experiment [7].

[4] For more information on CFARR, please visit http://www.chilbolton.rl.ac.uk/.
[5] Please consult http://badc.nerc.ac.uk/data/chilbolton for further information on the Chilbolton instruments.
[6] For more information on ARM sites and the ARM project, please visit http://www.arm.gov/about.
[7] For details of FAAM campaigns, please consult http://www.faam.ac.uk/public/campaigns/index.html.

Chapter 3

The retrieval algorithm

3.1 The inverse problem

Retrievals of cloud properties are an example of a solution to the 'inverse problem', as defined by Rodgers [2000*a*,*b*]. In an inverse problem, we wish to estimate the values of some set of parameters, $\mathbf{x}$, which cannot be measured directly. In order to do this, we make some set of measurements $\mathbf{y}$, which are related to $\mathbf{x}$ through the relationship $\mathbf{y} = \mathbf{F}(\mathbf{x})$. This relationship is then approximated by a 'forward model', $\mathbf{y} = \mathbf{f}(\mathbf{x})$. The solution is obtained by finding the inverse function $\mathbf{x} = \mathbf{f}^{-1}(\mathbf{y})$ and thus using the set of measurements $\mathbf{y}$ to calculate estimates of each of the parameters in the 'state vector', $\mathbf{x}$.

3.2 Retrieval method

The current version of the Oxford and Rutherford Appleton Aerosol and Cloud [ORAC] retrieval scheme [Poulsen et al., 2009] is designed to use information from five of the ATSR-2 nadir channels (0.67μm, 0.87μm, 1.6μm, 10.8μm and 12μm) simultaneously to retrieve the cloud fraction, cloud optical depth, cloud effective radius, cloud top pressure and the land/sea surface temperature on a pixel by pixel basis. This information is combined with *a priori* information on the state parameters in an Optimal Estimation [OE] framework. This allows error estimates to be calculated for each of the derived parameters, as well as a measure of the 'goodness of fit' of the solution to the observations. The details of the OE solution are discussed in section 3.5.

3.3 Origin of parameter information

Although the ATSR-2 and AATSR instruments were designed to perform accurate SST retrievals, they are also appropriate for the retrieval of cloud properties. Measurements taken in each channel will be moderated in some way by any cloud in the scene, as a result of the complex interaction between atmospheric radiation and the cloud, the surface and the atmosphere. The key features of this

interaction are summarised in the following paragraphs, which describe the origin of the information on each of the ORAC-ATSR cloud state parameters.

3.3.1 Cloud optical depth, τ

The cloud optical depth has a strong influence on measurements at all wavelengths. The visible reflectance measurements are directly related to the number of scattering objects in the scene and thus the cloud optical depth. A large range of optical depths can be detected using the visible channels, because these measurements do not saturate until very high values of optical depth are reached. In the thermal channels, the cloud optical depth is related to the thermal emission and absorption of the cloud. These both reach their maximum value at relatively low values of optical depth however, so the thermal channels can only provide optical depth information for optically thin clouds.

3.3.2 Cloud effective radius, $\mathrm{R_{eff}}$

Radiation interacts with cloud droplets through reflection, diffraction and absorption. These processes affect the fraction of the incident sunlight that is scattered into the ATSR-2 FOV by a cloud. Diffraction and reflection tend to scale with surface area, while absorption is related to the total volume of the droplets. The cloud effective radius, as defined in section 3.4.5 is thus related to the 'balance' between reflection, diffraction and absorption.

At visible wavelengths, where scattering dominates, there is very little internal absorption and so the effective radius only has a very small effect at a given optical depth. At IR wavelengths, the absorption dominates and the effect is similarly small. Channels that are sensitive to the cloud effective radius lie in the NIR/SIR where both absorption and scattering are important. In the ORAC-ATSR retrieval the 1.6μm channel provides the majority of the information on the cloud effective radius. In this channel a higher reflectance is observed for a smaller effective radius, at a fixed value of optical depth.

3.3.3 Cloud top pressure, $\mathrm{p_c}$

The cloud-top pressure is related to the temperature of a cloud and thus its IR emission. In addition, the cloud top pressure affects measurements in the visible channels by moderating the absorption of

the atmosphere above and below the cloud. In most situations however, this effect is negligibly small and only the thermal channels provide significant information.

3.3.4 Cloud fraction, f

In general, the ATSR-2 channels respond very differently to ‘clear-sky’ and ‘overcast’ conditions. As a result, the cloud fraction tends to dominate the signal in all channels. There are a small number of ‘difficult cases’ however; for example when thin clouds occur over a bright land surface (low contrast in the visible channels), or when low clouds exist at almost the same temperature as the land/sea surface (low contrast in the IR channels). Distinguishing between thick aerosol plumes and cloud and between ice cloud and a snowy surface can be difficult.

3.3.5 Cloud phase

Ice crystals and water droplets are usually differentiated by their different absorption characteristics in the 1.6μm channel. At a fixed optical depth and effective radius, ice cloud will have a higher transmission than water cloud because irregularly shaped ice crystals are less efficient at photon capture than spherical water droplets.

3.4 The forward model

At present, ORAC-ATSR is based on a decoupled three-layer radiative transfer [RT] model of the atmosphere in which a single cloud layer sits between two layers of ‘clear sky’, all overlying a Lambertian land or ocean surface. The properties of the cloud layer are calculated separately from the typical ‘clear sky’ properties for each pixel. Due to significant differences between the radiative transfer in the thermal [IR] and solar [VIS] channels two separate models are used for the different radiation sources. For most of the ATSR-2 channels, it is possible to use *either* the solar model *or* the thermal model, but in the 3.7μm [SIR] channel there are significant solar and thermal contributions. For that reason, the 3.7μm channel is not used in the ORAC-ATSR retrieval scheme.

3.4.1 Radiative transfer - ‘solar radiation stream’

The solar RT model is depicted in figure 12, neglecting the effect of atmospheric absorption. In this case, the first contribution to the TOA radiance is the direct **bidirectional reflectance**[8] (R_{BD}) of the cloud layer. For an optically thick cloud, the transmission is zero and this is the only contribution. More generally, the transmission through the cloud layer can be written as the sum of the **direct transmission**, (T_{DB}) and the **diffuse transmission** of scattered radiance (T_{FBD}), since any directionality of the radiance is lost on reflection by the underlying Lambertian surface.

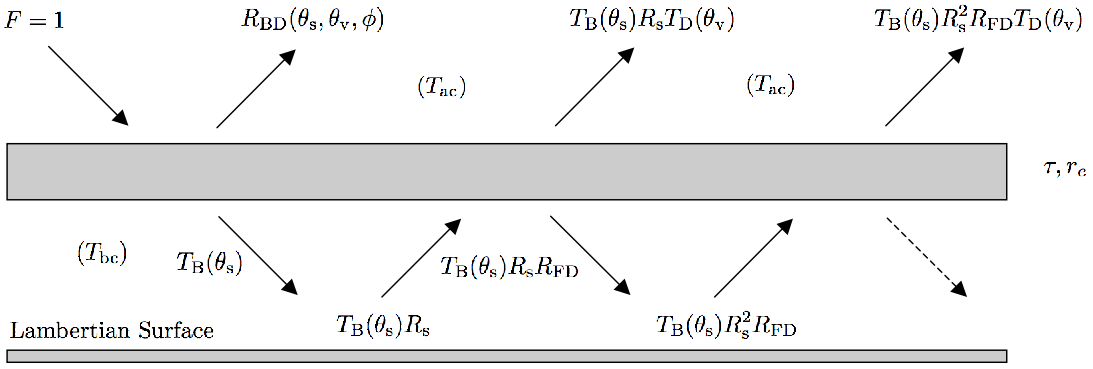

Figure 12: Cloud layer - surface interactions in the solar forward model.

The radiance reflected by the land or ocean surface $(T_{\mathrm{B}}(\theta_{\mathrm{s}})R_{\mathrm{s}})$ is assumed to be diffuse and is partially transmitted T_{D} by the cloud layer. This partial transmission forms the second component of the TOA radiance. The remaining terms arise due to multiple reflections between the cloud layer and the surface. Each of these terms is thus attenuated by a factor of $R_{\mathrm{S}}R_{\mathrm{FD}}$, where R_{FD} is the reflectance of the cloud layer to diffuse radiance and R_{S} is the surface reflectance. The total radiance measured at the instrument is thus given by:

$$\begin{aligned} R =& R_{\mathrm{BD}}(\theta_{\mathrm{s}}, \theta_{\mathrm{v}}, \phi) \\ &+ T_{\mathrm{B}}(\theta_{\mathrm{s}})R_{\mathrm{s}}T_{\mathrm{D}}(\theta_{\mathrm{v}}) \\ &+ T_{\mathrm{B}}(\theta_{\mathrm{s}})R_{\mathrm{s}}^2T_{\mathrm{D}}(\theta_{\mathrm{v}})R_{\mathrm{FD}} \\ &+ T_{\mathrm{B}}(\theta_{\mathrm{s}})R_{\mathrm{s}}^3T_{\mathrm{D}}(\theta_{\mathrm{v}})R_{\mathrm{FD}}^2 \\ &+ \cdots \end{aligned} \tag{5}$$

[8] In the RT model(s), transmission is treated as a fractional property and reflectance as a ‘sun-normalised reflectance’, $R = \pi I/F_0$, where I is the reflected radiance and F_0 is the solar irradiance.

We have defined θ_s as the solar zenith angle, θ_v as the satellite (instrumental view) zenith angle and ϕ as the relative azimuth angle between the Sun and the satellite. Equation 5 can be simplified to give:

$$R = R_{BD}(\theta_s, \theta_v, \phi) + T_B(\theta_s)T_D(\theta_v)R_s(1 + R_s R_{FD} + R_s^2 R_{FD}^2 + \cdots) \tag{6}$$

This result can be expressed as the limit of a geometric series:

$$R = R_{BD}(\theta_s, \theta_v, \phi) + \frac{T_B(\theta_s)T_D(\theta_v)R_s}{(1 - R_s R_{FD})} \tag{7}$$

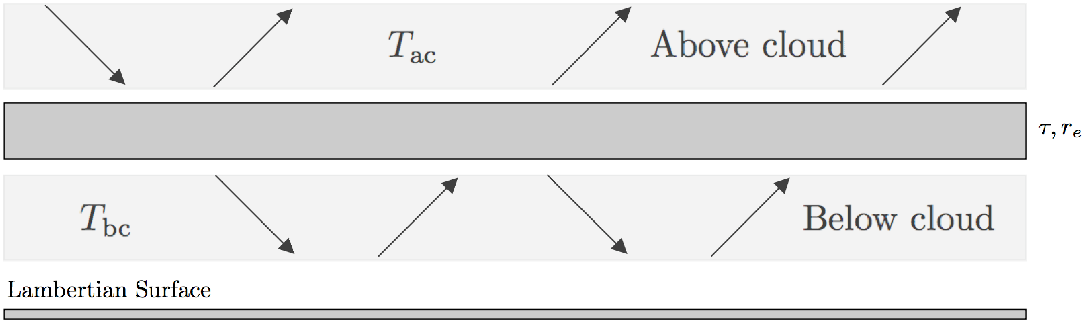

Figure 13: Cloud layer - atmosphere - surface interactions in the solar forward model.

Finally, it is necessary to include the transmittances of the atmospheric layers above and below the cloud deck, T_{ac} and T_{bc} respectively. The effect of these layers on the solar FM is depicted in figure 13. The TOA reflectance for a pixel completely covered by cloud is now given by:

$$R_{overcast} = T_{ac}(\theta_s)T_{ac}(\theta_v)\left[R_{BD}(\theta_s, \theta_v, \phi) + \frac{T_B(\theta_s)T_D(\theta_v)R_s}{(1 - R_s R_{FD} T_{bc}^2(\theta_d))}\right] \tag{8}$$

Again, θ_s is the solar zenith angle, θ_v the satellite (instrumental view) zenith angle and ϕ the relative azimuth angle between the Sun and the satellite. The angle θ_d gives a mean angle for the path of diffuse radiation to the instrument, defined as $66°$. For a completely clear pixel the solar reflectance at the satellite is given by the surface reflectance and the total atmospheric transmittance and so:

$$R_{clear\ sky} = R_s T_{tot}(\theta_s)T_{tot}(\theta_v) \tag{9}$$

where the total transmittance T_{tot} is given by

$$T_{\mathrm{tot}}(\theta) = \exp^{-(T_{\mathrm{ac}}+T_{\mathrm{bc}})} \tag{10}$$

Thus, the radiance measured in a pixel with fractional cloud cover f is given by:

$$R = fR_{\mathrm{overcast}} + (1-f)R_{\mathrm{clear\,sky}} \tag{11}$$

3.4.2 Radiative transfer - 'thermal radiation stream'

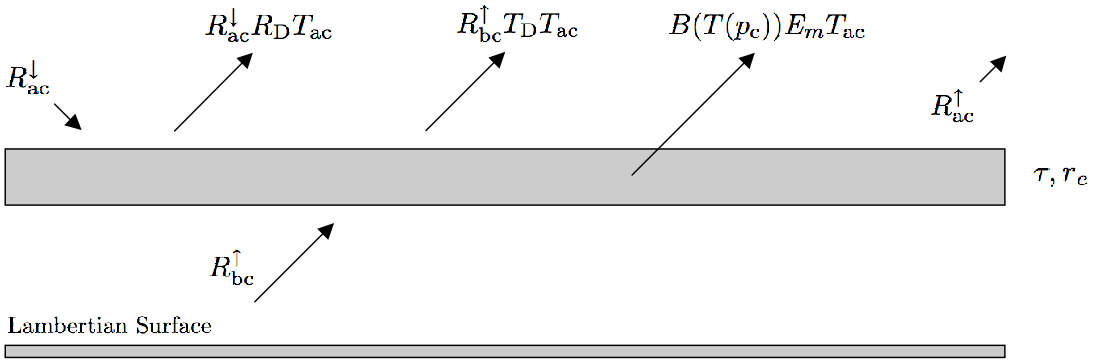

Figure 14: Cloud layer - atmosphere - surface interactions in the thermal forward model.

The thermal RT model is analagous to the solar model, again consisting of a single cloud layer lying between two layers of 'clear sky'. As shown in figure 14, there are four contributions to the TOA reflectance. The first two terms correspond to thermal emission of the upper atmospheric layer; the upwelling radiance, $R^{\uparrow}_{\mathrm{ac}}$ and the reflected downwelling radiance $R^{\downarrow}_{\mathrm{ac}}R_{\mathrm{D}}T_{\mathrm{ac}}$. The second two terms arise from the transmission of upwelling radiance from the atmospheric layer below the cloud layer, $R^{\uparrow}_{\mathrm{bc}}T_{\mathrm{D}}T_{\mathrm{ac}}$ and from the thermal emission of the cloud layer itself $B(T(p_{\mathrm{c}}))E_mT_{\mathrm{ac}}$. The total reflectance for the fully cloud covered pixel is thus given by:

$$R^{\uparrow}_{\mathrm{overcast}} = R^{\uparrow}_{\mathrm{ac}} + R^{\downarrow}_{\mathrm{ac}}R_{\mathrm{D}}T_{\mathrm{ac}} + R^{\uparrow}_{\mathrm{bc}}T_{\mathrm{D}}T_{\mathrm{ac}} + B(T(p_{\mathrm{c}}))E_mT_{\mathrm{ac}} \tag{12}$$

Thus, as in the solar case we can write the TOA reflectance for a partly cloudy pixel:

$$R^{\uparrow} = fR^{\uparrow}_{\mathrm{overcast}} + (1-f)R^{\uparrow}_{\mathrm{clear\,sky}} \tag{13}$$

3.4.3 Defining the 'clear sky' atmospheric properties

Atmospheric gas absorption Atmospheric gas absorption is calculated for each of the ATSR visible channels using the Moderate Resolution Atmospheric Transmission [MODTRAN] database [Brown et al., 2004] which provides climatological atmospheres of H_20, CO_2, O_3, N_2O, CO and CH_4, for a number of regions during Summer and Winter. The total gas absorption over the instrument band passes is convolved with the filter transmission functions for each channel. The data used in the retrieval scheme is based on the mid-latitude Summer profiles only. This approximation should not bring about a significant source of error since the ATSR channel windows are largely free of gas absorption features that vary over short timescales. In the solar channels, atmospheric gas absorption tends to be much weaker than scattering by cloud droplets.

Atmospheric radiative properties The radiative properties of the atmospheric layers above and below the cloud deck are calculated separately from the forward model using a version of the Radiative Transfer for the TIROS[9] Operational Vertical Sounder [RTTOV-7] package [Saunders et al., 1999]. RTTOV-7 employs a regression fitting method to calculate the spectral transmittance between a range of standard pressure levels and the top of the atmosphere, using reference temperature and humidity profiles obtained from the European Centre for Medium-Range Weather Forecasting [ECMWF, 2006]. The RTTOV package[10] has been comprehensively validated and subject to a great deal of development over recent years [Saunders et al., 2002].

Standard pressure levels (mbar)									
0.1	2	0.5	1.0	1.5	2	3	4	5	7
10	15	20	25	30	50	60	70	85	100
115	135	150	200	250	300	350	400	430	475
500	570	620	670	700	780	850	920	950	1000

Table 3: Standard pressure levels.

Using the RTTOV package, $T_{\rm ac}$, $T_{\rm bc}$, $R_{\rm ac}$ and $R_{\rm bc}$ can be calculated at a wide range of pressure levels for each of the required channels. A large number of levels are used to ensure an accurate interpolation. The data is stored in radiative transfer model [RTM] files which can be accessed

[9] The Television Infra-Red Observation Satellite Program [TIROS] is the name given to a series of NASA weather satellites. The TOVS instrument flies on the 'new generation' of TIROS satellites, TIROS-N, the first of which was launched in 1978.

[10] Please visit http://www.metoffice.gov.uk/research/interproj/mwpsaf/rtm for more information on RTTOV

quickly during the retrieval process.

The attenuation optical depths provided by RTTOV are calculated for a nadir path, so a simple scaling law is applied to calculate the transmission of a slanted atmospheric path. We have:

$$\tau(\theta) = \tau(0) \times \sec(\theta) \tag{14}$$

and therefore

$$T(\theta) = \tau(0)^{\sec(\theta)} \tag{15}$$

Since the 'clear sky' atmospheric transmission tends to be relatively high, this approximation is not expected to be a significant source of error.

3.4.4 Defining the surface properties

Over both land and ocean pixels, an effective Lambertian surface must be calculated for incorporation into the RT model. Over land, this surface is calculated using the MODIS BRDF product [Scatterfield et al., 2004] developed by Wanner et al. [1997]. Data from the year 2002 is used as a reference, because the ATSR-2 mission pre-dates the launch of MODIS. Individual missing pixels are assigned a nearest neighbour value, but *'a priori'* values are used to fill larger gaps. The product is averaged onto a sinusoidal grid at the required resolution.

The technique developed by Sidran [1981] is used to calculate the albedo over the ocean. The degree to which the sea surface is 'roughened' by wind is modelled using the Fresnel equations and Cox and Munk statistics [Cox and Munk, 1954*a*,*b*]. The 'roughness' of the ocean is related to the number of specular reflections occuring from its surface and thus the albedo [Sidran, 1981]. Surface wind speed data over the ocean is obtained from the European Centre for Medium-Range Weather Forecasting [ECMWF, 2006].

Sun-glint Over some ocean regions, the surface contribution to the visible TOA radiance can become very large, due to the specular reflection of sunlight from the ocean surface. This 'sun-glint' principally affects measurements in the nadir view, due to its geometry and the reduced transmission in the forward view. At present, cloud retrievals are not undertaken in the 'sun-glint' domain. An example of the effect of 'sun-glint' is shown in section 5.2.

3.4.5 Defining the cloud properties

Water clouds In the ORAC-ATSR retrieval scheme, water cloud droplets are treated as spheres and their scattering properties calculated using Mie theory [Mie, 1908; Wiscombe, 1980]. The optical properties are averaged over a modified gamma distribution. The frequency of finding a droplet of radius r for a mode radius $r\mathrm{m}$ is given by the relation:

$$n(r) = 2.373 \times r^6 exp^{(-6r/r_{\mathrm{m}})} \tag{16}$$

The effective radius is defined as the area weighted mean radius of the cloud droplets:

$$R_{\mathrm{eff}} = \frac{\int_0^\infty r^3 n(r) dr}{\int_0^\infty r^2 n(r) dr} \tag{17}$$

In this case we have $R_{\mathrm{eff}} = 1.5 \times r_{\mathrm{m}}$. Refractive index data for water droplets is taken from Irvin and Pollock [1969]; values at the central wavelength of each channel are used.

Ice clouds The scattering properties of an ice cloud can be modelled by a distribution of ice crystals with known refractive indices. In this scheme the 'Uncinus cirrus' distribution of Takano and Liou [1989] is used, along with refractive index data calculated by Warren [1984] .

The ice cloud properties are then calculated using a combination of ray-tracing and T-Matrix methods as described by Macke et al. [1995]. Typically, ray tracing methods are used for larger ice crystals, while T-matrix methods are used for the smaller crystals.

3.4.6 Deriving the Cloud Radiative Transfer Properties [CRP]

The Discrete Ordinances Radiative Transfer package [DISORT] [Olesen, 2005; Stamnes et al., 1988] is used to generate look up tables [LUTs] of cloud radiative properties given the viewing geometry, the cloud phase, the cloud optical depth and the effective droplet size. The required radiative properties are shown in table 4.

1. **Beam bi-directional reflection** R_{BD} is the direct reflection of the solar beam from the cloud deck. It is a function of the full viewing geometry.

Quantity	Channels	Effective radius (r_{eff})	Optical depth (τ)	Solar zenith (θ_{s})	View zenith (θ_{v})	Relative azimuth (ϕ)
Beam bi-directional reflectance, R_{BD}	VIS	✓	✓	✓	✓	✓
Direct beam transmission, T_{BD}	VIS	✓	✓		✓	
Diffuse transmission, T_{FBD}	VIS	✓	✓	✓		
Diffuse transmission, T_{D}	ALL	✓	✓		✓	
Diffuse reflection, R_{FD}	VIS	✓	✓			
Diffuse reflection, R_{D}	IR	✓	✓		✓	
Emmisivity, ϵ_{c}	IR	✓	✓		✓	

Table 4: Cloud radiative properties required by the ORAC-ATSR forward model(s).

2. **Direct beam transmission** T_{BD}, is the fraction of the solar beam transmitted through the cloud layer.

3. **Diffuse beam transmission** T_{FBD} is the fraction of the solar beam transmitted through the cloud layer having undergone multiple scattering. This quantity is strictly a function of the full viewing geometry, but a flux version integrated over the solar zenith and relative azimuth angles is used here. This is done because a Lambertian surface is used in the solar forward model, and so any angular dependence of the diffuse beam transmission will be lost on reflection. T_{FBD} and T_{BD} are added to give the total *beam* transmission through the cloud, denoted as T_{B}.

4. **Diffuse transmission** T_{D} is the transmission of isotropic radiation through the cloud layer, which is dependent on the instrument zenith angle θ_{v}.

5. **Diffuse reflection** R_{FD} represents the reflection of isotropic radiation by the cloud layer in the solar model. This is treated as a flux quantity, again because any angular dependence is lost on reflection from the Lambertian surface.

6. **Diffuse reflection** R_{D} represents the reflection of isotropic radiation by the cloud layer in the thermal model. It is a function of the full viewing geometry.

7. **Emissivity** ϵ_{c} represents the efficiency with which Planck radiation is emitted by the cloud. It is dependent on the instrument zenith angle.

Parameter	Minimum value	Maximum value	Point spacing	Number of points
$log(\tau)$	0	2.408	0.301	9
r_{eff} (water)	1μm	23μm	2μm	12
r_{eff} (ice)	20μm	50μm	10μm	4
θ_{s}	0°	90°	10°	10
θ_{v}	0°	90°	10°	10
ϕ	0°	180°	18°	11

Table 5: The ORAC-ATSR LUT points in phase space.

The structure of each of the LUT dimensions in 'parameter space' is given in table 5. The value of optical depth used in the LUTs corresponds to the optical thickness of the cloud at $0.55\mu m$. For each of the channels used in the ORAC retrieval the optical depth, τ^{i} is given by the relation:

$$\tau^{\mathrm{i}} = \tau^{55} \times \frac{Q^{\mathrm{i}}_{\mathrm{ext}}}{Q^{55}_{\mathrm{ext}}} \tag{18}$$

where the Q^{i} is the extinction coefficient in channel i. The current version of the ORAC retrieval uses a linear interpolation scheme to establish the reflectance values and their derivatives from the LUTs. A new bicubic interpolation scheme has been developed for the next version of the retrieval and is described in the following chapter.

3.4.7 The solar gradient model

In order to invert the Forward Model [FM] using the Levenburg-Marquardt algorithm, which employs a combination of steepest descent and Newtonian descent, it is necessary to calculate the derivatives of the TOA radiance with respect to the state parameters. In addition, the gradients of the TOA radiance with respect to model parameters such as the surface reflectance are used to calculate the forward model 'error budget'. This 'error budget' gives the relative contribution made to the total retrieval error by each of the model parameters.

The derivative of the radiance equation with respect to the fractional cloud cover f is given by:

$$\frac{\partial R}{\partial f} = R_{\mathrm{overcast}} - R_{\mathrm{clear\ sky}} \tag{19}$$

and with respect to some other state variable x:

$$\frac{\partial R}{\partial x} = \frac{\partial R_{\text{overcast}}}{\partial x} + (1-f)\frac{\partial R_{\text{clear sky}}}{\partial x} \tag{20}$$

This notation becomes cumbersome when derivatives of R_{overcast} are taken. Here, we denote R_{overcast} by $R_{\bullet}$, omit any explicit angular dependencies and combine the above cloud two-path transmittances to give $T = T_{\text{ac}}(\theta_{\text{s}})T_{\text{ac}}(\theta_{\text{v}})$:

$$R_{\bullet} = T\left[R_{\text{BD}} + \frac{T_{\text{B}}T_{\text{D}}R_{\text{s}}T_{\text{BC}}^2}{1 - R_{\text{s}}R_{\text{FD}}T_{\text{BC}}^2}\right] \tag{21}$$

We can simplify the expression even further, using the variable S to denote the cloud-surface interaction terms:

$$S = \frac{T_{\text{B}}T_{\text{D}}R_{\text{s}}T_{\text{BC}}^2}{1 - R_{\text{s}}R_{\text{FD}}T_{\text{BC}}^2} \tag{22}$$

We therefore have

$$R_{\bullet} = T\left[R_{\text{BD}} + S\right] \tag{23}$$

The derivatives of this expression with respect to each of the cloud parameters (x_{i}), the 'clear sky' transmittances $(T_{\text{ac}}/T_{\text{bc}})$ and the surface reflectance (R_{s}) are given below. Primes are used as a shorthand for a partial derivative with respect to the current variable. The gradient values for the cloud radiative properties are supplied to the FM by the LUT interpolation routines. For a full derivation of the gradients given here, please consult Watts et al. [1998].

- **Gradient of $R_{\bullet}$ with respect to effective radius (r_{eff}):**

$$\frac{\partial R_{\bullet}}{\partial r_{\text{eff}}} = T\left[R'_{\text{BD}} + \frac{S\left[T_{\text{D}}T'_{\text{B}} + T'_{\text{D}}T_{\text{B}}\right]}{T_{\text{D}}T_{\text{B}}} + \frac{R_{\text{s}}T_{\text{bc}}^2R'_{\text{FD}}}{\left[1 - R_{\text{s}}R_{\text{FD}}T_{\text{bc}}^2\right]}\right] \tag{24}$$

- **Gradient of $R_{\bullet}$ with respect to optical depth (τ):**

$$\frac{\partial R_{\bullet}}{\partial \tau} = T\left[R'_{\text{BD}} + \frac{S\left[T_{\text{D}}T'_{\text{B}} + T'_{\text{D}}T_{\text{B}}\right]}{T_{\text{D}}T_{\text{B}}} + \frac{R_{\text{s}}T_{\text{bc}}^2R'_{\text{FD}}}{\left[1 - R_{\text{s}}R_{\text{FD}}T_{\text{bc}}^2\right]}\right] \tag{25}$$

- **Gradient of $R_{\bullet}$ with respect to surface reflectance (R_{s}):**

$$\frac{\partial R_{\bullet}}{\partial R_{\text{s}}} = TS\left[\frac{1}{R_{\text{s}}} + \frac{R_{\text{FD}}T_{\text{bc}}^2R'_{\text{FD}}}{\left[1 - R_{\text{s}}R_{\text{FD}}T_{bc}^2\right]}\right] \tag{26}$$

- **Gradient of $R_{\bullet}$ with respect to atmospheric transmission (T_{ac}):**

$$\frac{\partial R_{\bullet}}{\partial T_{\mathrm{ac}}} = -R\left[\sec(\theta_s) + \sec(\theta_v)\right] \tag{27}$$

- **Gradient of $R_{\bullet}$ with respect to atmospheric transmission (T_{bc}):**

$$\frac{\partial R_{\bullet}}{\partial T_{\mathrm{bc}}} = 2TST_{\mathrm{bc}}\left[\frac{1}{T_{\mathrm{bc}}^2} + \frac{R_{\mathrm{FD}}R_{\mathrm{s}}}{[1 - R_{\mathrm{s}}R_{\mathrm{FD}}T_{\mathrm{bc}}^2]}\right] \tag{28}$$

- **Gradient of $R_{\circ}$ with respect to surface reflectance (R_{s}):**

$$\frac{\partial R_{\circ}}{\partial R_{\mathrm{s}}} = T(\theta_{\mathrm{s}})T(\theta_{\mathrm{v}}) \tag{29}$$

- **Gradient of $R_{\circ}$ with respect to the total transmission (T):**

$$\frac{\partial R_{\circ}}{\partial T} = -R_0[\sec(\theta_s) + \sec(\theta_v)] \tag{30}$$

3.4.8 The thermal gradient model

The thermal gradient model is entirely analogous to the solar gradient model and the same notation is employed in this section. The expression for the TOA radiance (equation 13) is written:

$$R^{\uparrow} = fR_{\bullet}^{\uparrow} + (1 - f)R_{\circ}^{\uparrow} \tag{31}$$

and therefore

$$\frac{\partial R^{\uparrow}}{\partial \tau} = f \frac{\partial R^{\uparrow}_{\bullet}}{\partial \tau} \tag{32}$$

$$\frac{\partial R^{\uparrow}}{\partial r_{\mathrm{eff}}} = f \frac{\partial R^{\uparrow}_{\bullet}}{\partial r_{\mathrm{eff}}} \tag{33}$$

$$\frac{\partial R^{\uparrow}}{\partial p_{\mathrm{c}}} = f \frac{\partial R^{\uparrow}_{\bullet}}{\partial p_{\mathrm{c}}} \tag{34}$$

$$\frac{\partial R^{\uparrow}}{\partial T_{\mathrm{s}}} = f \frac{\partial R^{\uparrow}_{\bullet}}{\partial T_{\mathrm{s}}} + (1-f) \frac{\partial R^{\uparrow}_{\circ}}{\partial T_{\mathrm{s}}} \tag{35}$$

The expressions for the cloudy-sky FM gradient with respect to each of the state parameters follow from equation 12:

- **Gradient of $R_{\bullet}$ with respect to cloud optical depth (τ):**

$$\frac{\partial R^{\uparrow}_{\bullet}}{\partial \tau} = T_{\mathrm{ac}} \left[R^{\uparrow}_{\mathrm{bc}} \frac{\partial T_{\mathrm{D}}}{\partial \tau} + B(T(p_{\mathrm{c}})) \frac{\partial E_{\mathrm{m}}}{\partial \tau} + R^{\downarrow}_{\mathrm{ac}} \frac{\partial R_{\mathrm{D}}}{\partial \tau} \right] \tag{36}$$

- **Gradient of $R_{\bullet}$ with respect to cloud effective radius (r_{eff}):**

$$\frac{\partial R^{\uparrow}_{\bullet}}{\partial r_{\mathrm{eff}}} = T_{\mathrm{ac}} \left[R^{\uparrow}_{\mathrm{bc}} \frac{\partial T_{\mathrm{D}}}{\partial r_{\mathrm{eff}}} + B(T(p_{\mathrm{c}})) \frac{\partial E_{\mathrm{m}}}{\partial r_{\mathrm{eff}}} + R^{\downarrow}_{\mathrm{ac}} \frac{\partial R_{\mathrm{D}}}{\partial r_{\mathrm{eff}}} \right] \tag{37}$$

- **Gradient of $R_{\bullet}$ with respect to cloud top pressure (p_{c}):**

$$\begin{aligned} \frac{\partial R^{\uparrow}_{\bullet}}{\partial p_{\mathrm{c}}} =& \frac{\partial R^{\uparrow}_{\mathrm{ac}}}{\partial p_{\mathrm{c}}} + T_{\mathrm{ac}} \left[\frac{\partial R^{\uparrow}_{\mathrm{bc}}}{\partial p_{\mathrm{c}}} T_{\mathrm{D}} + \frac{\partial B(T(p_{\mathrm{c}}))}{\partial p_{\mathrm{c}}} E_{\mathrm{m}} + \frac{\partial R^{\downarrow}_{\mathrm{ac}}}{\partial p_{\mathrm{c}}} R_{\mathrm{D}} \right] \\ &+ \frac{\partial T_{\mathrm{ac}}}{\partial p_{\mathrm{c}}} \left[R^{\uparrow}_{\mathrm{bc}} T_{\mathrm{D}} + B(T(p_{\mathrm{c}})) E_{\mathrm{m}} + R^{\downarrow}_{\mathrm{ac}} R_{\mathrm{D}} \right] \end{aligned} \tag{38}$$

3.5 Inversion by Optimal Estimation

The basic principle of Optimal Estimation [OE] is to identify the retrieved state with the greatest probability, conditional on the observations and any *a priori* information. The conditional probability

of some state $\mathbf{x}$ is represented as follows:

$$P(\mathbf{x}) = P\left(\mathbf{x}|\mathbf{y}, \mathbf{x}_{\mathrm{b}}, \mathbf{b}\right) \tag{39}$$

where $\mathbf{x}$ is the state vector, $\mathbf{y}$ is the measurement vector, $\mathbf{x}_{\mathrm{b}}$ is the *a priori* information on $\mathbf{x}$ and $\mathbf{b}$ is a vector including the ancillary data required by the forward model, known as 'forward model parameters'. In the ORAC-ATSR retrieval these parameters include temperature and humidity profiles, as well as surface reflectance and emissivity. The full state vector, $\mathbf{x}$, is defined as

$$\mathbf{x} = \left[\, \tau, r_{\mathrm{eff}}, p_{\mathrm{c}}, f, T_{\mathrm{s}} \,\right] \tag{40}$$

Likewise, the model parameter vector, $\mathbf{b}$, is defined as

$$\mathbf{b} = \left[\, T_{\mathrm{z}}, H_{\mathrm{z}}, R_{\mathrm{s}}, \epsilon_{\mathrm{s}} \,\right] \tag{41}$$

where T_{z} and H_{z} represent the temperature and humidity profiles respectively, R_{s} represents the surface reflectance and ϵ_{s} the surface emissivity.

3.5.1 Definition of the retrieval 'cost', J

The errors in the measurements, *a priori* and model parameters are assumed to be normally distributed with zero mean and variance and are represented by the vectors $\mathbf{S}_y$, $\mathbf{S}_x$ and $\mathbf{S}_b$ respectively. As a result, the conditional probability can be written in the quadratic form:

$$\begin{aligned} P(\mathbf{x}) \propto & \exp\left[-(\mathbf{y}(\mathbf{x}) - \mathbf{y}_{\mathrm{m}})\mathbf{S}_{\mathrm{y}}^{-1}(\mathbf{y}(\mathbf{x}) - \mathbf{y}_{\mathrm{m}})^T\right] \\ & \times \exp\left[-(\mathbf{x} - \mathbf{x}_{\mathrm{a}})\mathbf{S}_{\mathrm{x}}^{-1}(\mathbf{x} - \mathbf{x}_{\mathrm{a}})^T\right] \\ & \times \exp\left[-(\mathbf{b}_{\mathrm{t}} - \mathbf{b})\mathbf{S}_{\mathrm{b}}^{-1}(\mathbf{b}_{\mathrm{t}} - \mathbf{b})^T\right] \end{aligned} \tag{42}$$

where $\mathbf{y}(\mathbf{x})$ is the vector of measurements predicted by the forward model for the state $(\mathbf{x})$, $\mathbf{y}_m$ denotes the actual measurement vector and $\mathbf{b}_t$ has been written for the (unknown) true values of the model parameters. The terms represent the weighted deviations of the current state $(\mathbf{x})$ from the measurement vector $(\mathbf{y}_{\mathrm{m}})$, the *a priori* state $(\mathbf{x}_{\mathrm{a}})$ and the model parameters $(\mathbf{b}_{\mathrm{t}})$ respectively.

Maximising probability is equivalent to minimising the negative logarithm and thus in the retrieval the 'cost', J, is minimised, where

$$\begin{aligned} J(\mathbf{x}) &= (\mathbf{y}(\mathbf{x}) - \mathbf{y}_{\mathrm{m}})\mathbf{S}_{\mathrm{y}}^{-1}(\mathbf{y}(\mathbf{x}) - \mathbf{y}_{\mathrm{m}})^T \\ &+ (\mathbf{x} - \mathbf{x}_{\mathrm{a}})\mathbf{S}_{\mathrm{x}}^{-1}(\mathbf{x} - \mathbf{x}_{\mathrm{a}})^T \\ &+ (\mathbf{b}_{\mathrm{t}} - \mathbf{b})\mathbf{S}_{\mathrm{b}}^{-1}(\mathbf{b}_{\mathrm{t}} - \mathbf{b})^T \end{aligned} \tag{43}$$

The expression is minimised with respect to the state variable $\mathbf{x}$, in order that the derivative of J is independent of the third term and $\mathbf{b}$ does not enter the solution. Since there is no explicit dependence on $\mathbf{b}$, the cost function to be minimised can be reduced to:

$$\begin{aligned} J(\mathbf{x}) &= (\mathbf{y}(\mathbf{x}) - \mathbf{y}_{\mathrm{m}})\mathbf{S}_{\mathrm{y}}^{-1}(\mathbf{y}(\mathbf{x}) - \mathbf{y}_{\mathrm{m}})^T \\ &+ (\mathbf{x} - \mathbf{x}_{\mathrm{a}})\mathbf{S}_{\mathrm{x}}^{-1}(\mathbf{x} - \mathbf{x}_{\mathrm{a}})^T \end{aligned} \tag{44}$$

The first and second derivatives of $\mathbf{J}$ with respect to $\mathbf{x}$ are given by:

$$J' = \frac{\partial J}{\partial \mathbf{x}} = \mathbf{K}_{\mathrm{x}}^T\mathbf{S}_{\mathrm{y}}^{-1}(\mathbf{y}(\mathbf{x}) - \mathbf{y}_{\mathrm{m}}) + \mathbf{S}_{\mathrm{x}}^{-1}(\mathbf{x} - \mathbf{x}_{\mathrm{a}}) \tag{45}$$

$$J'' = \frac{\partial^2 J}{\partial \mathbf{x}^2} = \mathbf{K}_{\mathrm{x}}^T\mathbf{S}_{\mathrm{y}}^{-1}\mathbf{K}_{\mathrm{x}} + \mathbf{S}_{\mathrm{x}}^{-1} \tag{46}$$

The weighting function matrix $\mathbf{K}_{\mathrm{x}}$ is composed of the forward model gradients, as defined in section 3.4. It has dimensions n_{y} by n_{x}, where n_{y} is the number of measurements and n_{x} the number of state variables. The expression for J'' results from the assumption that $\mathbf{K}_{\mathrm{x}}$ is independent of $\mathbf{x}$ and thus that the radiative transfer is linear in $\mathbf{x}$. Although this is only the case near the solution (where J is quadratic), the approximation will hold because this is exactly the region in which J'' is employed in the minimisation (see section 3.5.2).

The characteristics of the minimisation problem are as follows:

1. Continuous first and second derivatives of J (with respect to $\mathbf{x}$) exist. This implies that it is possible to use fastest-descent algorithms that use the local gradient. Such algorithms tend to approach the minimum faster than other methods, particularly when the initial 'guess' is far from the solution.

2. Multiple minima are unlikely. As a result, excessive domain searches to avoid them need not be employed.

3. In the region of the solution, J is likely to be approximately quadratic while significant deviations from this behaviour are expected elsewhere. This will make a quick convergence from a poor starting position unlikely.

3.5.2 Minimising the cost function

As a result of the characteristics outlined in the previous section, the Levenburg-Marquardt algorithm [Levenburg, 1944; Marquardt, 1963] is used to minimise the cost function. This algorithm uses a weighted combination of steepest descent and Newtonian descent methods, dependent on the characteristics of the cost function. Thus, the robustness of the steepest descent method far from the solution is combined with the efficiency of Newtonian descent method in the region of the solution (where J is quadratic).

Starting at some 'first guess' state $\mathbf{x}_0$, the state vector is perturbed by a series of steps $\delta\mathbf{x}_0 ... \delta\mathbf{x}_\mathrm{n}$. Each step $(\delta\mathbf{x}_\mathrm{n})$ depends on the current value of the cost function $(J(\mathbf{x}))$. When the retrieval solution is found, the retrieved state is denoted by $\hat{\mathbf{x}}$ while $\hat{\mathbf{y}}$ denotes the final estimate of the measurement vector $\mathbf{y}$ computed from $\hat{\mathbf{x}}$ using the FM.

The steepest descent algorithm The direction of the steepest 'downward' gradient in the cost function at some point $\mathbf{x}$ in phase space is defined by the vector $-J'(\mathbf{x})$. This vector is likely to be in the direction of the minimum, although a move of $-J'(\mathbf{x})$ through state space may 'overshoot' the minimum itself. The step is therefore typically scaled by some value α, so that $\delta\mathbf{x} = -\alpha J'(\mathbf{x})$. If the step results in a decrease in the cost, a step with a higher value of α can be attempted and likewise if the step results in an increased cost a step with a smaller value of α can be attempted. As $\mathbf{x}$ approaches the solution $(\hat{\mathbf{x}})$, the gradient will become small. As a result, steepest descent is often slow to 'converge' on the final solution. It is, however, highly robust.

The Newtonian descent algorithm This algorithm is used to find the root of the equation $J'(\mathbf{x}) = 0$. The Newtonian step is therefore defined as $\delta\mathbf{x} = -J'(\mathbf{x})/J''(\mathbf{x})$. If the cost function is quadratic in the region of $\mathbf{x}$, this method will find the solution in just one iteration. On the other

hand, where the behaviour of the cost function is far from quadratic, the method can easily lead to a step in the wrong direction, due to variations in the sign of $J''(\mathbf{x})$

The Levenburg-Marquardt algorithm As stated, this method employs a combination of steepest descent far from the solution, and Newtonian iteration close to it. The dependence of the step size on the cost function is as follows:

$$\delta\mathbf{x} = -(J''(\mathbf{x}) + \alpha I)^{-1} J'(\mathbf{x}) \tag{47}$$

where I is the unit matrix (of size $n_{\mathrm{x}} \times n_{\mathrm{x}}$) and α is the 'control variable'. When $\alpha > J''$ the step tends to approximate steepest descent; when $\alpha > J''$ the step tends to approximate Newtonian descent.

The average of the diagonals of $J''(\mathbf{x}_0)$ is used to define a value for the initial step α_0:

$$\alpha_0 = MQ_{\mathrm{start}} \times \frac{Tr(J''(\mathbf{x}_0))}{n_{\mathrm{x}}} \tag{48}$$

If a step results in a *decrease* in $J(\mathbf{x})$, the step is taken and α is decreased, thus changing the behaviour of the next step *towards Newtonian descent*:

$$\alpha_{n+1} = \frac{\alpha_n}{MQ_{\mathrm{step}}} \tag{49}$$

If a step results in an *increase* in $J(\mathbf{x})$, the step is **not** taken. Before another step is attempted α is increased (thus changing the behaviour of the minimisation *towards steepest descent*) as follows:

$$\alpha_{n+1} = \alpha_n \times MQ_{\mathrm{step}} \tag{50}$$

The control parameters MQ_{start} and MQ_{step} have default values of 0.001 and 10 respectively.

Parameter scaling There is a great deal of variation in the sensitivity of the RT model to the different parameters in the state vector. For example, the cloud top pressure has a very weak effect on the observed visible reflectance measurements when compared to the cloud fraction, as shown in table 6. Thus, the weighting function matrix $\mathbf{K}_{\mathrm{x}}$ will contain elements covering a wide range

State Parameter	'Unit' change in parameter	Equivalent change in visible reflectance in channel i
$\mathbf{p}_c$	1mbar	$\sim 0.01\%$
$\mathbf{f}$	1	$\sim 60\%$

Table 6: The sensitivity of the solar FM to the state parameters $\mathbf{p}_c$, $\mathbf{f}$.

of orders of magnitude. Although this is scientifically valid, $\mathbf{K}_x^{-1}$ will often be ill-conditioned as a result. In order to avoid this problem it is appropriate to *scale* a number of the state parameters.

It is observed that converting the cloud fraction term to a percentage coverage increases the number of retrievals that converge. This linear scaling does not effect the location of the minimum of the cost function or its shape in phase space; it only has the effect of changing the size of the step parameter in the early stages of the minimisation.

Using a non-linear scaling factor will also leave the location of the minimum of the cost function unchanged. However in this case the shape of the minimum will be distorted, which can increase the likelihood of convergence. In the ORAC-ATSR scheme the optical depth is scaled logarithmically, since the forward model response is more linear when optical depth is expressed as a logarithm.

State parameter boundaries The state space in which the minimisation is undertaken is physically bounded in many dimensions, as shown in table 7. These 'state limits' prevent the retrieval of

State parameter	Upper limit	Lower limit
f	0	1
τ	0	255
R_{eff} (water)	1μm	23μm
R_{eff} (ice)	20μm	50μm
p_c (water)	100hPa	1000hPa
p_c (ice)	100hPa	1000hPa
T_s	-	-

Table 7: Limits on the 'state parameter space' in the ORAC-ATSR cloud retrieval.

unphysical values. A good example is the cloud fraction, which must lie between 0 and 1. Rather than reject steps $\delta\mathbf{x}_i$ that cause one of the state parameters to cross a 'boundary', the value of that parameter is 'clamped' at the boundary value and the minimisation problem is effectively reduced by one dimension. This means that boundary values are readily retrieved for the cloud fraction, without affecting the step size $\delta\mathbf{x}_i$ and thus the minimisation in the other parameters.

Phase changes During the retrieval process phase changes are driven by the value of the effective radius. If the 'first guess' state $\mathbf{x}_0$ for some scene consists of water cloud, then the retrieval will change the cloud phase to ice if a step $\delta\mathbf{x}$ is taken that increases the effective radius beyond the boundary value of 23 μm. Likewise, if a step $\delta\mathbf{x}$ is taken reducing the effective radius of an ice cloud to below 20 μm, the phase will be changed to water. For each retrieved pixel, a maximum of three phase changes is allowed.

Convergence criteria If the parameter x_i is poorly constrained in some particular situation, the cost function will be almost flat in the x_i dimension. In this case, the minimisation can oscillate or prove unstable, despite the minimum in the cost function having been located. As a result, the iteration process is stopped when the change in cost between successive iterations becomes negligibly small. At present, the retrieval is treated as having converged when $\delta\mathbf{J}_\mathrm{n} < 0.05$. This convergence criterion prevents any instability in the minimisation procedure.

3.5.3 Quality control information

Some means of quality control on the retrieved product is a key aspect of any inverse problem. Three key quality control diagnostics are provided using the optimal estimation framework:

- **Cost**, J, is a measure of the 'goodness of fit' of the solution to the measurements and any *a priori* constraints. A high cost is indicative of a scene that is poorly represented by the forward model, for example a scene containing multi-layered cloud.
- **Forward model parameter errors** give an indication of the error in each of the retrieved parameters. Scenes with a low cost, but high parameter errors are likely to result when there is insufficient information in the signal. A scene with a very low cloud fraction would be prone to large model parameter errors, for example.
- **Number of iterations**. A failure to converge indicates no solution can been found, while instant convergence suggests that the signal does not contain sufficient information on the state.

Model fit The cost at the solution, $J(\hat{\mathbf{x}})$, is a measure of the 'quality' of the solution to within the errors assumed for measurements and any *a priori* data. If, at the solution, none of the state variables

$\hat{x}_{\mathrm{i}}$ deviate from their *a priori* values $x_{\mathrm{a_i}}$ by significantly more than the *a priori* error ($S_{\mathrm{x_i}}$) and none of the FM predicted measurements $\hat{y}_{\mathrm{i}}$ deviate from the actual observations y_{i} by significantly more than their expected noise ($S_{\mathrm{y_i}}$), then $J(\mathbf{x})$ will be of order $n_{\mathrm{y}} + n_{\mathrm{x}}$ (where n_{y} is the number of measurements and n_{x} the number of variables in the state vector).

As a result of the lack of *a priori* information, there are generally *fewer* degrees of freedom than $n_{\mathrm{x}} + n_{\mathrm{y}}$. The cloud fraction, for example, can contribute barely any of its expected $\mathbf{S}_{\mathrm{x}}$ value to J. As a result, an acceptable solution is likely to have a cost of the order of $n_{\mathrm{x}} + n_{\mathrm{y}} - n_{\mathrm{b}}$, where n_{b} is the number of state variables that is bounded but lacking any significant *a priori* information.

The retrieval keeps separate records of the measurement and *a priori* contributions to the cost (J_{y} and J_{x} respectively). In the case of a particularly high cost, the elements of $\hat{\mathbf{y}} - \mathbf{y}$ and $\hat{\mathbf{y}} - \mathbf{x}_{\mathrm{a}}$ can be examined to find the measurement or state variable responsible.

Because J depends on the estimation of values for $\mathbf{S}_y$ and $\mathbf{S}_x$, the cost of a 'good' retrieval is unlikely to be exactly $n_{\mathrm{x}} + n_{\mathrm{y}} - n_{\mathrm{b}}$ as expected. A value that is too low suggests an overestimation of the measurement errors, while a value that is too high suggests either an underestimation of the noise levels or an insufficiently 'tight' convergence criterion.

3.5.4 Linear error analysis

Optimal estimation allows rigorous errors to be calcuated on each of the retrieved state parameters $\hat{x}_{\mathrm{i}}$. If the radiative transfer model is assumed to be linear in the vicinity of the solution, it can be shown[11] that the solution for the minimum of the cost function:

$$\begin{aligned} J(\mathbf{x}) = &(\mathbf{y}(\mathbf{x}) - \mathbf{y}_{\mathrm{m}})\mathbf{S}_{\mathrm{y}}^{-1}(\mathbf{y}(\mathbf{x}) - \mathbf{y}_{\mathrm{m}})^T \\ &+ (\mathbf{x} - \mathbf{x}_{\mathrm{a}})\mathbf{S}_{\mathrm{x}}^{-1}(\mathbf{x} - \mathbf{x}_{\mathrm{a}})^T \\ &+ (\mathbf{b}_{\mathrm{t}} - \mathbf{b})\mathbf{S}_{\mathrm{b}}^{-1}(\mathbf{b}_{\mathrm{t}} - \mathbf{b})^T \end{aligned} \tag{51}$$

is found where

$$\hat{\mathbf{x}} = (\mathbf{S}_{\mathrm{x}}^{-1} + \mathbf{K}_{\mathrm{x}}^T\mathbf{S}_{\mathrm{y}}^{-1}\mathbf{K}_{\mathrm{x}})^{-1}(\mathbf{S}_{\mathrm{x}}^{-1}\mathbf{x}_{\mathrm{a}} + \mathbf{K}_{\mathrm{x}}^T\mathbf{S}_{\mathrm{y}}^{-1}\mathbf{y}) \tag{52}$$

[11] Please consult Rodgers [2000*b*] for a complete derivation.

The 'inversion operator', defined as $\mathbf{D}_{\mathrm{y}} = \partial\hat{\mathbf{x}}/\partial\hat{\mathbf{y}}$ is thus given by:

$$\mathbf{D}_{\mathrm{y}} = (\mathbf{S}_{\mathrm{x}}^{-1} + \mathbf{K}_{\mathrm{x}}^{T}\mathbf{S}_{\mathrm{y}}^{-1}\mathbf{K}_{\mathrm{x}})^{-1}\mathbf{K}_{\mathrm{x}}^{T}\mathbf{S}_{\mathrm{y}}^{-1} \tag{53}$$

Following the convention of Rodgers [2000*b*], three error sources are identified: 'null space', or *a priori* smoothing error, measurement error and model parameter error. These errors are expressed in the form of the covariance matrices $\mathbf{S}_{\mathrm{N}}$, $\mathbf{S}_{\mathrm{M}}$, and $\mathbf{S}_{\mathrm{S}}$ respectively.

Null space error The null space error $\mathbf{S}_{\mathrm{N}}$ is given by the expression:

$$\mathbf{S}_{\mathrm{N}} = (\mathbf{D}_{\mathrm{y}}\mathbf{K}_{\mathrm{x}} - \mathbf{I})\mathbf{S}_{\mathrm{x}}(\mathbf{D}_{\mathrm{y}}\mathbf{K}_{\mathrm{x}} - \mathbf{I})^{T} \tag{54}$$

'Null space' errors arise when there is a lack of information in the measurement system. For example, over a scene containing thick cloud, the ATSR-2 signal will contain almost no information from the land/sea surface; thus the retrieved surface temperature $\mathbf{T}_{\mathrm{s}}$ will be subject to a large 'null space' error. This can be seen intuitively from equation 54, since both $\mathbf{D}_{\mathrm{y}}$ and $\mathbf{K}_{\mathrm{x}}$ will tend to zero, leaving $\mathbf{S}_{\mathrm{N}} \approx \mathbf{S}_{\mathrm{x}}$.

Measurement mapping error The measurement 'mapping' error $\mathbf{S}_{\mathrm{M}}$ expresses the effect of errors in the ATSR-2 measurements on the retrieval solution:

$$\mathbf{S}_{\mathrm{M}} = \mathbf{D}_{\mathrm{y}}\mathbf{S}_{\mathrm{y}}\mathbf{D}_{\mathrm{y}}^{T}. \tag{55}$$

Model parameter mapping error The model parameter mapping error $\mathbf{S}_{\mathrm{S}}$ expresses the effect of errors in the forward model parameters on the retrieval solution. In the ORAC-ATSR scheme this error is included in the measurement error matrix $\mathbf{S}_{y}$.

$$\mathbf{S}_{\mathrm{S}} = (\mathbf{D}_{\mathrm{y}}\mathbf{K}_{\mathrm{b}})\mathbf{S}_{\mathrm{b}}(\mathbf{D}_{\mathrm{y}}\mathbf{K}_{\mathrm{b}})^{T} \tag{56}$$

Error on the retrieved state $(\hat{\mathrm{x}})$ The total error on $\hat{\mathbf{x}}$ is thus given by the sum of the null space and measurement errors:

$$\hat{\mathbf{S}}_{\mathrm{tot}} = (\mathbf{S}_{\mathrm{x}}^{-1} + \mathbf{K}_{x}^{T}\mathbf{S}_{\mathrm{y}}^{-1}\mathbf{K}_{\mathrm{x}})^{-1} \tag{57}$$

As stated, all of the error terms are expressed as covariance matrices. The correlations implied by the off-diagonal terms in these matrices can be used to interpret the information content of the measurements. It is unrealistic to routinely output the full covariance matrices for all three error sources in the operational code. The ORAC-ATSR output contains only the square root of the diagonals for the total error, $\mathbf{S}_{\mathrm{T}}$. It is important to note that error estimate applies to each state parameter separately; a high expected error in one parameter does not necessarily imply a high error in another. The error estimate is conditional upon the correct solution being found using an accurate set of fixed model parameters.

3.6 Statistical constraints on the retrieval

The solution $\hat{\mathbf{x}}$ is constrained by the quality of the measurements and *a priori* information. These constraints are taken into account using the OE method, by the error covariance matrices S_{x} and S_{y} respectively. The details of how these matrices are calculated is outlined in the following sections.

3.6.1 *A priori* information

At present, very little *a priori* information is provided to the ORAC-ATSR retrieval. Global daytime/nighttime *a priori* values are set for each of the state parameters, for ice and water clouds. Given this lack of *a priori* information, the diagonals of the *a priori* error covariance matrix, S_{x} are effectively set to infinity. This means that the *a priori* will not bias the retrieval of parameters for which there is some signal in the ATSR-2 measurement. The *a priori* information will only be incorporated in the solution when there is no signal in the ATSR-2 measurement, and in this case the total error $\hat{\mathbf{S}}_{\mathrm{tot}}$ will be approximately equal to the *a priori* error $(\sim \infty)$. The *a priori* values used in ORAC-ATSR and their errors are given in table 8. There is no correlation between the *a priori* errors used in the ORAC-ATSR scheme, so the covariance matrix S_{x} has zero off-diagonal elements.

Parameter:	τ	r_{eff}	p_{c}	f
Water cloud value	1.2	8 μm	800 Pa	1
Ice cloud value	1.2	30 μm	400 Pa	1
A priori error	3×10^{8}	1×10^{8} μm	1×10^{8} Pa	1×10^{8}

Table 8: *A priori* values used in the ORAC-ATSR cloud retrieval.

'First guess' values It is important to distinguish the role of 'first guess values' from the *a priori* information. These values are used as the initial state for the iteration process $\mathbf{x}_0$, but **do not** provide any statistical constraint on the solution. In ORAC-ATSR, the *a priori* data is used to set the first guess state, but this need not necessarily be the case. The 'first guess' information should rarely have any effect on the retrieval except to alter the number of iterations require before the solution is reached. In rare 'difficult' scenes however it is possible that a different choice of first guess value may result in convergence where a previous value did not.

3.6.2 Measurement errors

The measurement error covariance matrix, $\mathbf{S}_\mathrm{y}$, is made up of the radiometric noise in the ATSR-2 measurements, the forward model parameter errors $\mathbf{S}_\mathrm{S}$ and any limitations in the forward model itself. These contributions are discussed briefly below, for a more detailed discussion consult [Watts, 2000; Watts et al., 1998].

- **Instrument noise** in each of the ATSR-2 channels used in the retrieval is characterised by a NEΔT. For each of the visible channels, the NEΔT is converted to a 'noise equivalent percentage reflectance' before being incorporated into $\mathbf{S}_\mathrm{y}$, while for the thermal channels it is incorporated directly.

- **Limitations in the forward model** are likely to cause errors that will be highly correlated between different channels. Very little is known of the nature of these errors however, so they are assumed to be uncorrelated.

- **Model parameter errors** are mapped onto the measurement errors as follows:

$$\mathbf{S}_\mathrm{yb} = \mathbf{K}_\mathrm{b}\mathbf{S}_\mathrm{b}\mathbf{K}_\mathrm{b}^T \tag{58}$$

  This 'equivalent model parameter noise' [EQMPN] is then added directly to the covariance matrix $\mathbf{S}_\mathrm{y}$. In ORAC-ATSR, $\mathbf{S}_\mathrm{yb}$ includes errors on all the RT model parameters except the surface emissivity (ϵ_s) and ECMWF profiles $(T(z)/H(z))$.

Chapter 4

The ORAC-ATSR cloud products

In order to develop and improve the ORAC-ATSR cloud retrieval it is necessary to understand the conditions under which the algorithm performs 'well' and under which it performs 'poorly'. To some extent, this can be achieved by analysing the quality control parameters generated by the retrieval, but these parameters can only yield the success of the retrieval scheme within the accuracy of the forward model. In order to validate the retrieval scheme, it is necessary to compare the retrieved products with cloud data generated using different instruments and retrieval methods. Over the past year, a combination of these approaches has been taken to inform the future development of the ORAC-ATSR retrieval, as described in the following sections.

4.1 The GEWEX cloud assessment study

The Global Energy and Water Cycle Experiment [GEWEX] is a core project of the World Climate Research Programme [WCRP] with the principal aim of developing models capable of reproducing the past and predicting the future behaviour of the global hydrological cycle[12]. In 2005 a Cloud Assessment [CA] study was initiated as part of the GEWEX project, in order to assess the reliability of long-term cloud data from a variety of satellite instruments[13]. To date, monthly mean maps of high (< 440 Pa), mid-level ($440 < 680$ Pa) and low (> 680 Pa) cloud properties from a number of instruments have been compared and their seasonal variations analysed over six latitude bands [Stubenrauch et al., 2009]. ORAC-ATSR data has been submitted to the next stage of the project, in which a greater variety of parameters will be investigated in the same way, as well as using probability density functions at a resolution of up to 1×1 km. Some examples of the products that have been submitted to the GEWEX CA study are included below.

The ORAC-ATSR cloud assessment data Monthly mean values of cloud fraction, cloud top pressure, cloud optical depth, cloud effective radius and cloud water path for high, mid-level and low clouds were prepared on a 1×1 km grid for the GEWEX CA study. In each case, quality control

[12] For more information on GEWEX, please consult http://www.gewex.org/.
[13] Please consult http://climserv.ipsl.polytechnique.fr/gewexca/ for more information.

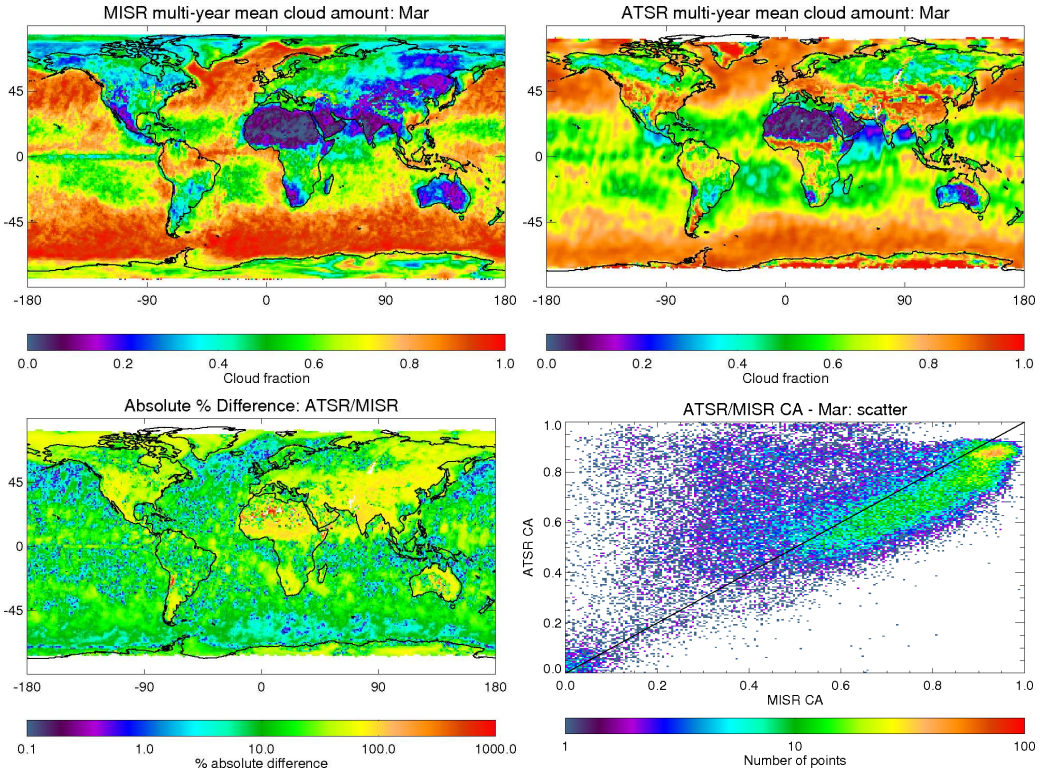

Figure 15: A comparison of ORAC-ATSR and MISR cloud fraction data for a 'mean March'. The bottom left hand plot shows the absolute percentage difference between the MISR and ATSR images and the bottom right plot shows the scatter of the retrieved cloud fraction in each $1^\circ \times 1^\circ$ pixel.

thresholds were applied to the data, which are summarised in table 9. Each threshold was selected in order to provide a balance between data quality and statistical significance (quantity of data). Over the ocean a $5^\circ \times 5^\circ$ smoothing filter was passed through the data in order to reduce the standard error on the mean values reported in each $1^\circ \times 1^\circ$ pixel.

Parameter	Constraint
Retrieval cost J	< 30
Error on cloud top pressure, p_c	< 400 Pa
Error on cloud optical depth, τ	$< 50 + (0.8 \times \tau)$
Error on cloud effective radius, r_{eff}	< 10 μm

Table 9: Quality control constraints on the ORAC-ATSR GEWEX cloud assessment data.

It is important to note that in order to properly account for the monthly mean cloud fraction, even failed retrievals must be considered. Pixels in which the retrieval fails are assigned an *a priori* cloud fraction of 60%. The relative high, mid-level and low cloud fractions on the other hand, can only be calculated using pixels for which there is a cloud top pressure retrieval. No quality control is applied to any of the cloud fraction data, since it would be likely to introduce some bias.

MISR and ATSR cloud fraction Figure 15 shows a comparison between the MISR [Diner et al., 1998] and ATSR cloud fraction products. Since there is no significant overlap between the operation periods of ATSR-2 and MISR, the comparison has been undertaken for a 'mean March', using ORAC-ATSR data from 1997-2000 and MISR data from 2001-2007. Over the ocean, there is a good agreement between the two (of the order of $\sim 10\%$), but the ATSR cloud fraction is generally lower in regions of persistent cloud cover. The MISR data shows a much greater land/sea contrast than that of ORAC-ATSR and the agreement between the two products is particularly poor over land in the northern hemisphere. Over Greenland and Antarctica it is likely that the ORAC-ATSR algorithm is detecting surface ice as cloud, but the reason for the large discrepancy between the two datasets over land in the northern midlatitudes is not clear.

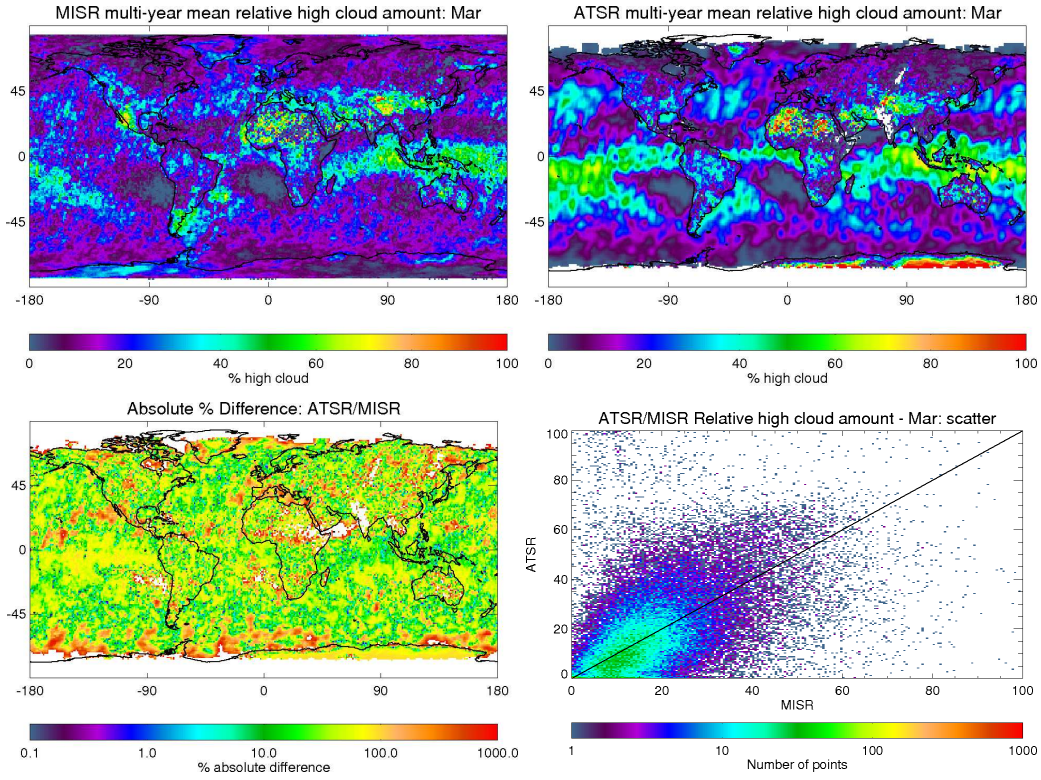

Figure 16: A comparison of MISR and ATSR relative high cloud fraction data for a 'mean March'. The bottom left hand plot shows the absolute percentage difference between the MISR and ATSR images and the bottom right plot shows the scatter of the retrieved relative high cloud fraction in each $1^\circ \times 1^\circ$ pixel.

Given the important radiative effects of high clouds, it is interesting to also compare the relative fraction of high cloud retrieved by each instrument. The global distribution of high cloud seems to be very consistent between the two instruments, although ORAC-ATSR tends to retrieve a smaller relative high cloud fraction than MISR. Again, there is a clear indication over Antarctica that snow

covered surfaces lead to difficulties in the ORAC-ATSR retrieval scheme.

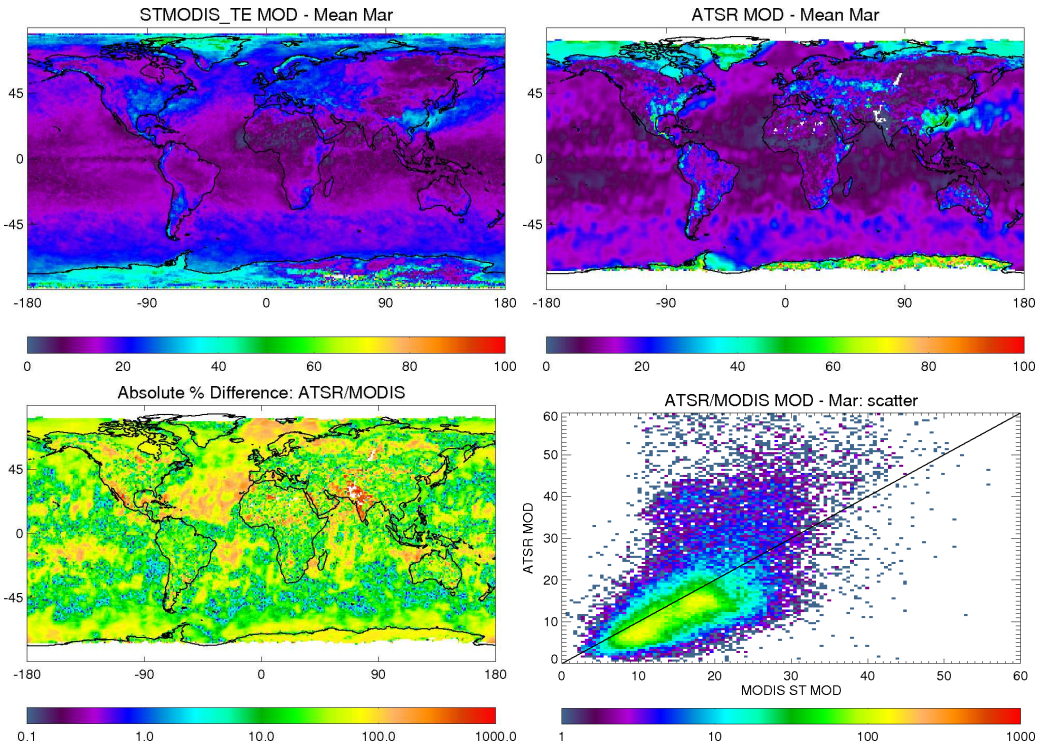

Figure 17: A comparison of MODIS and ATSR mid-level cloud optical depth data for a ‘mean March’. The bottom left hand plot shows the absolute percentage difference between the MODIS and ATSR images and the bottom right plot shows the scatter of the retrieved mid-level cloud optical depth in each $1^\circ \times 1^\circ$ pixel.

Mid-level cloud optical depth Figure 17 shows a comparison of the mid-level cloud optical depth derived by the MODIS science team [MODIS-ST] retrieval [Platnick et al., 2003] and by ORAC-ATSR. Again, data for a ‘mean March’ is used, incorporating MODIS Terra data from 2001-2008. The spatial distribution of mid-level cloud optical depth observed by the two instruments is very similar, but ORAC-ATSR tends to detect a lower optical depth in most regions. Sea ice retrieved as cloud is likely to account for the high optical depth reported by ORAC-ATSR over the ocean at latitudes greater than 60°N. This effect is not observed in the MODIS data because the MODIS instrument has an operational sea ice and surface snow/ice detection algorithm, which is used to ‘mask’ such pixels from the cloud retrieval [Hall et al., 1998]. The potential for the development of a similar mask for the ORAC-ATSR retrieval is discussed in section 5.4.

Cloud water path Two parameters of particular interest to cloud modellers are the cloud ‘ice water path’ and ‘liquid water path’. Cloud water path is used as a parameter in large scale global cir-

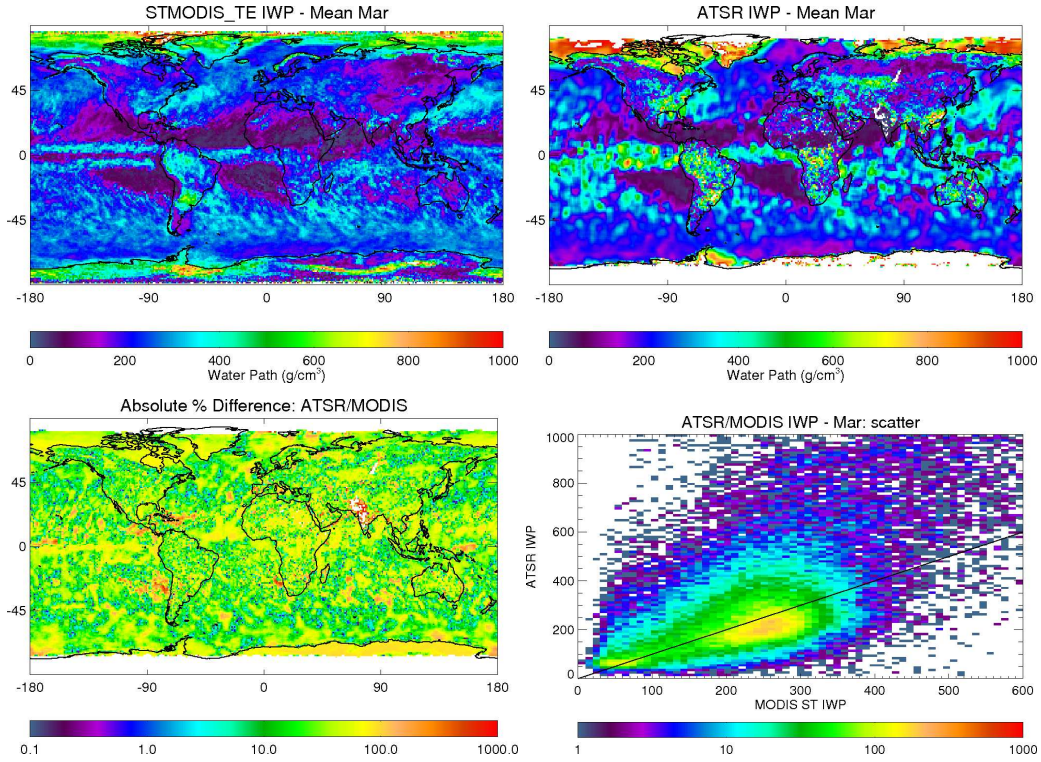

Figure 18: A comparison of MODIS and ATSR cloud ice water path data for a 'mean March'. The bottom left hand plot shows the absolute percentage difference between the MODIS and ATSR images and the bottom right plot shows the scatter of the retrieved ice water path in each $1^\circ \times 1^\circ$ pixel.

culation models [GCMs], such as those used by the IPCC to predict future climate change [Solomon et al., 2007]. Climatologies of cloud water path produced by satellite instruments have a key role to play in the validation of these models.

In the ORAC-ATSR scheme, the cloud liquid water path and cloud ice water path are calculated using the retrieved cloud optical depth and effective radius:

$$\text{Cloud water path} = \frac{4.0 \times \rho_{\mathrm{i}}}{3.0 \times q_{\mathrm{i}}} \times \text{Effective Radius} \times \text{Optical Depth} \tag{59}$$

where ρ_{i} is the density of water/ice cloud respectively and q_{i} is a parameter related to the extinction coefficient of the water/ice particles integrated over the ATSR-2 channels. The density of water droplets is assumed to be 1.0 kg m^{-3} and the value of q_{water} to be 2.119; the density of ice cloud crystals is assumed to be 0.917 kg m^{-3} and the value of q_{ice} to be 2.0.

A comparison of the ATSR and MODIS cloud ice water path is given in figure 18. Both the ATSR and MODIS images show a similar spatial distribution of ice water path. The majority of pixels lie close to the $y = x$ line, although at high values of liquid water content ($>$ 400 g cm^{-3}) ORAC-ATSR

predicts values $\sim 40\%$ greater than MODIS. There is evidence of poor retrievals by both instruments over the ocean at latitudes greater than 60°, although it is particularly clear in the ATSR data.

4.2 ORAC-ATSR quality control information

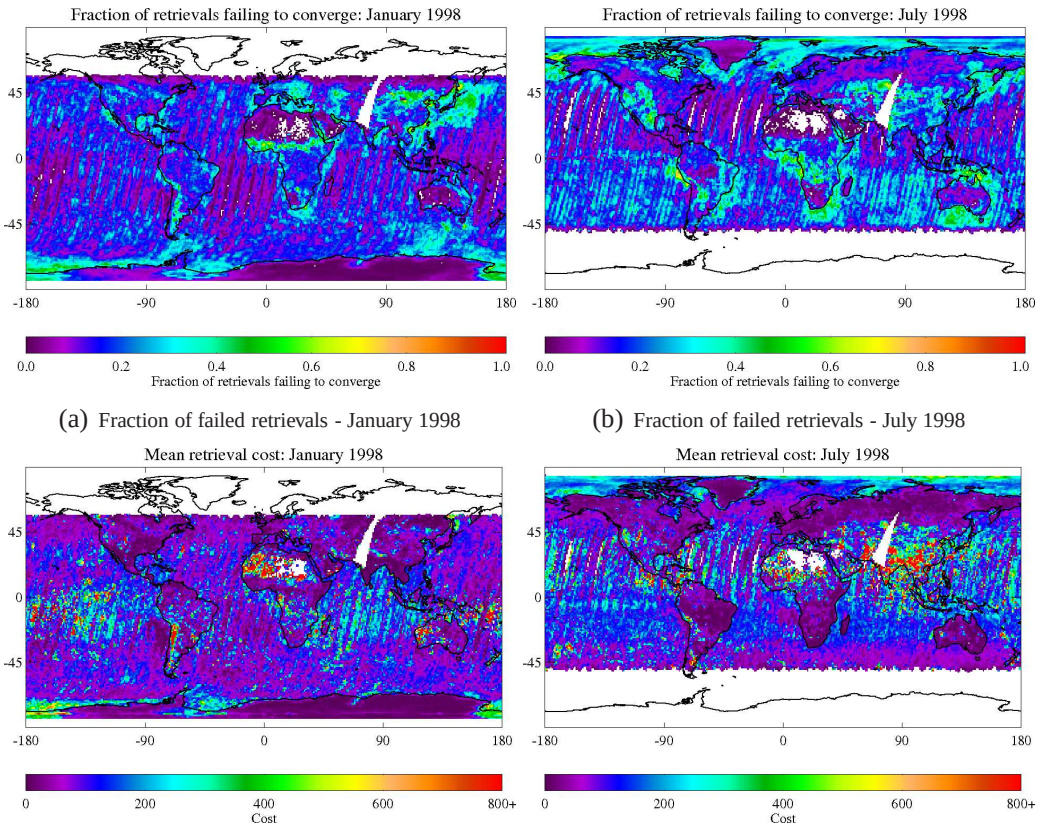

(a) Fraction of failed retrievals - January 1998

(b) Fraction of failed retrievals - July 1998

(c) Mean retrieval cost - January 1998

(d) Mean retrieval cost - July 1998

Figure 19: The fraction of retrievals that fail to converge and the mean retrieval cost, mapped at a $1° \times 1°$ resolution, for January and July 1997.

Figures 19(a) and (b) show the fraction of ORAC-ATSR retrievals that fail to converge, mapped at $1° \times 1°$ resolution, for the months of January and July 1997 respectively. On a global scale, $\sim 20\%$ of the retrievals fail to converge but much higher failure rates are observed in some regions. The effects of sea ice are likely to be responsible for the high fraction of failed retrievals in the Arctic Ocean, the Sea of Okhotsk and the Ross Sea. There is also evidence that the retrieval is less likely to converge over mountainous regions: the Andes appear to correspond to a high failure rate ($\sim 40\%$) in figure 19(a) and in figure 19(b) the Himalyas, the Rocky mountains and the Sierra Nevada correpond to high failure rates. Increasing the number of retrievals that converge is a key target for future versions of ORAC-ATSR.

Figures 19(c) and (d) show the mean retrieval cost for January and July 1997. Regions bordering the Sahara show a consistent high cost, which is likely to be due to a poor characterisation of the surface reflectance. The high cost observed in the region of India during July could be due to the presence of multi-layered clouds; a study of multilayer cloud distributions by Heidinger and Pavolonis [2005] reports a high occurence of multilayered cloud in the region during July. The areas of high cost near the equator in January could also be the result of multilayered cloud systems. Close to the poles, high costs are likely to result from sea ice ‘contamination’ of the scene. In January, a high cost is observed over the Andes and over the Victoria desert in Australia; this is once again likely to be the result of a poor characterisation of the surface reflectance.

Chapter 5

Improving the ORAC-ATSR Cloud Retrieval

In the previous chapter, several limitations were identified in the present version of the ORAC-ATSR cloud retrieval scheme. In this chapter, recent work to improve the retrieval algorithm is described and strategies for future algorithm development are put forward.

5.1 New interpolation schemes for ORAC-ATSR

Figure 20 shows histograms of the retrieved values of water cloud optical depth, effective radius and pressure for four orbits from the 1st of January 2001. 'Spikes' are clearly visible in each histogram, corresponding to values that are preferentially retrieved for each parameter. In each case, the location of these 'spikes' is correlated with the locations of the LUT points (see table 5). There is no scientific reason for these 'spikes'; they arise as an artefact of the retrieval process itself.

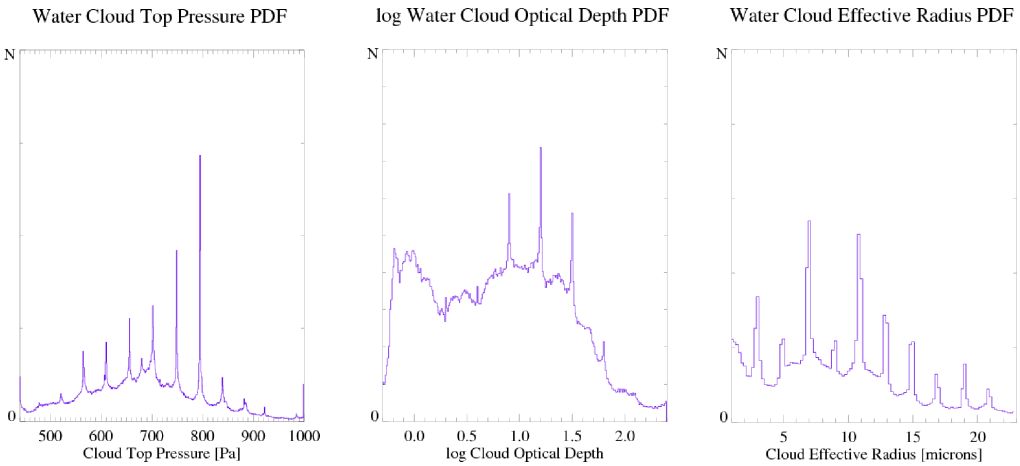

Figure 20: Histograms of the water cloud top pressure, water cloud optical depth and water cloud effective radius as retrieved by ORAC-ATSR for four orbits from the 1st January 2001.

It might be expected that the histogram 'spikes' would correspond to retrievals with a high cost or a large parameter error, but this is not the case. The retrieved values that fall in the 'spikes' do however correspond to a larger than typical number of iterations. This is illustrated in figure 21, which shows the mean number of retrieval iterations as a function of retrieved water cloud effective radius.

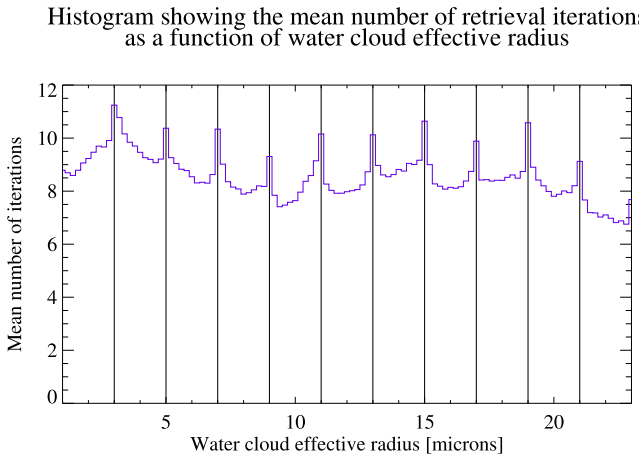

Figure 21: Histogram showing the relationship between the retrieved water cloud effective radius and the number of retrieval iterations.

The correlation between the number of iterations and the preferential retrieval of certain parameter values indicates that the origin of the parameter 'spikes' lies in the inversion of the FM using the Levenburg-Marquardt algorithm. The Levenburg-Marquardt inversion is driven by the FM gradient, which is calculated using derivatives derived from the LUTs of cloud radiative properties and the external RTM files.

5.1.1 Development of new interpolation schemes for ORAC-ATSR

At present, linear interpolation methods are used throughout the FM: atmospheric transmission and emission data from the RTM files are interpolated to the current cloud top pressure level and LUTs of cloud radiative properties are interpolated to the current viewing/solar geometry, cloud effective radius and cloud optical depth. This linear interpolation results in FM gradients that are discontinuous at the LUT/pressure level boundaries.

Over the past year, two new interpolation schemes have been developed[14] for the ORAC-ATSR FM that are able to provide a continuous FM gradient. It was expected that these schemes would produce parameter histograms free from the 'spikes' observed in the ORAC-ATSR data retrieved operationally.

- In the first scheme, a cubic spline interpolation is used to estimate the values of atmospheric transmission and emission at the current pressure level. A linear scheme is then used to inter-

[14] Interpolation routines developed by Press et al. [1987, 1996], have been used as the basis for the schemes described here.

polate the LUTs of cloud radiative properties to the current geometry, before a bicubic spline is used to interpolate in the final two dimensions; cloud optical depth and cloud effective radius. This scheme is referred to as the **'bicubic scheme'**.

- The second scheme is analogous to the first, but the bicubic interpolation used to interpolate the LUTs in cloud optical depth and cloud effective radius is replaced by two separate cubic spline interpolations. This scheme is referred to as the **'2×cubic spline scheme'** or the **'2D cubic spline scheme'**.

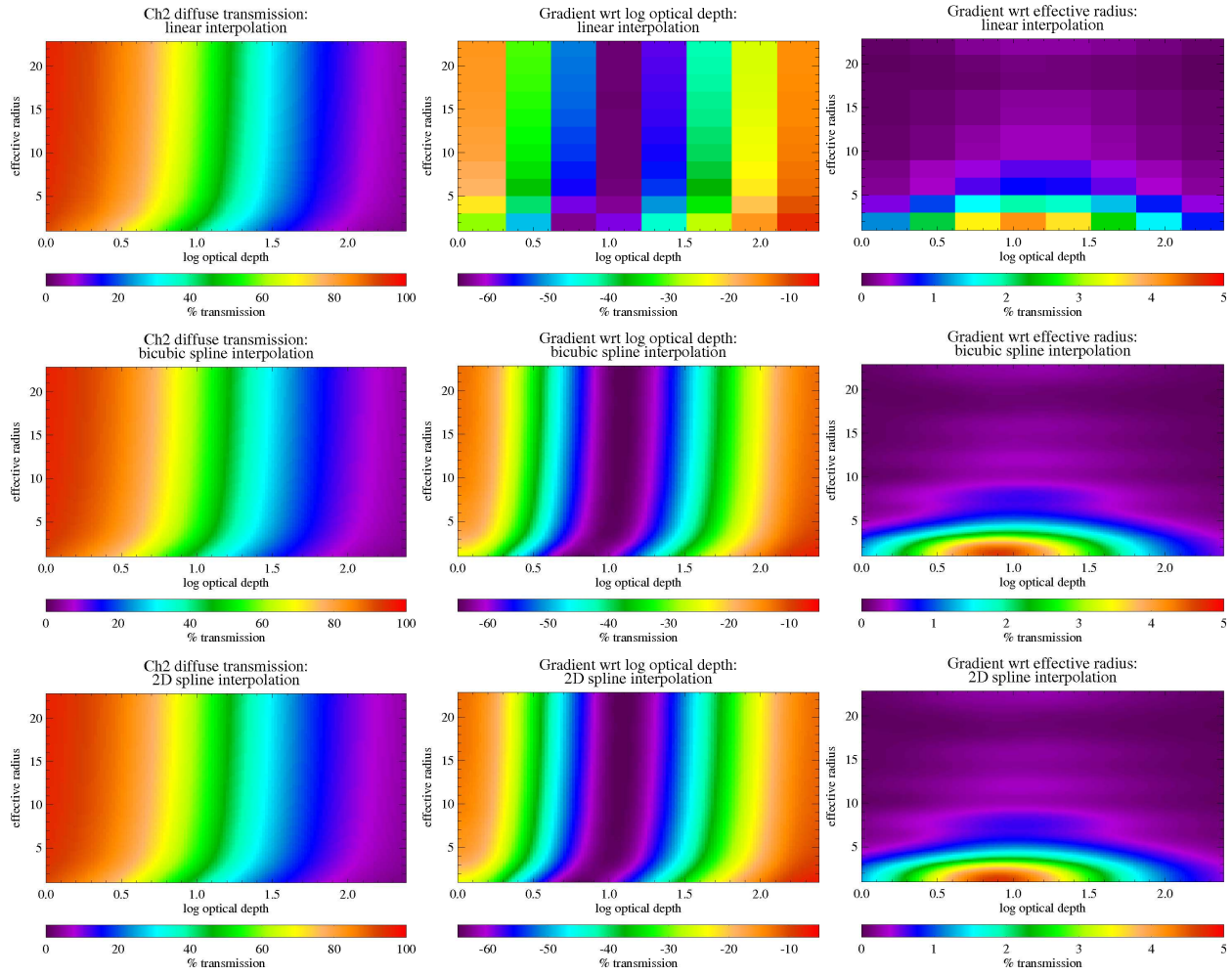

Figure 22: An example of the interpolation schemes tested in ORAC-ATSR. In each case, the LUT for diffuse transmission (T_{D}) in the 0.67μm channel has been interpolated onto a uniform 120×120 point grid in parameter space. The interpolated transmission values are shown in the first column, the second column shows the transmission gradient with respect to optical depth and the final column shows the gradient with respect to effective radius. Each row corresponds to a different interpolation scheme.

Examples of the application of the original linear interpolation scheme, the bicubic interpolation scheme and the 2D spline interpolation scheme to the calculation of the diffuse transmission of a

water cloud at 0.67μm are given in figure 22. While the interpolation method does not have a great effect on the transmission calculated at any point in parameter space, it has a clear effect on the gradient with respect to the optical depth and effective radius. The smooth gradients calculated by the two new interpolation schemes are more likely to lead to a quick convergence of the ORAC-ATSR retrieval and to eliminate the artefacts in the retrieved cloud data. Four orbits were processed using each scheme and histograms plotted of each of the cloud parameters, as shown in figure 23.

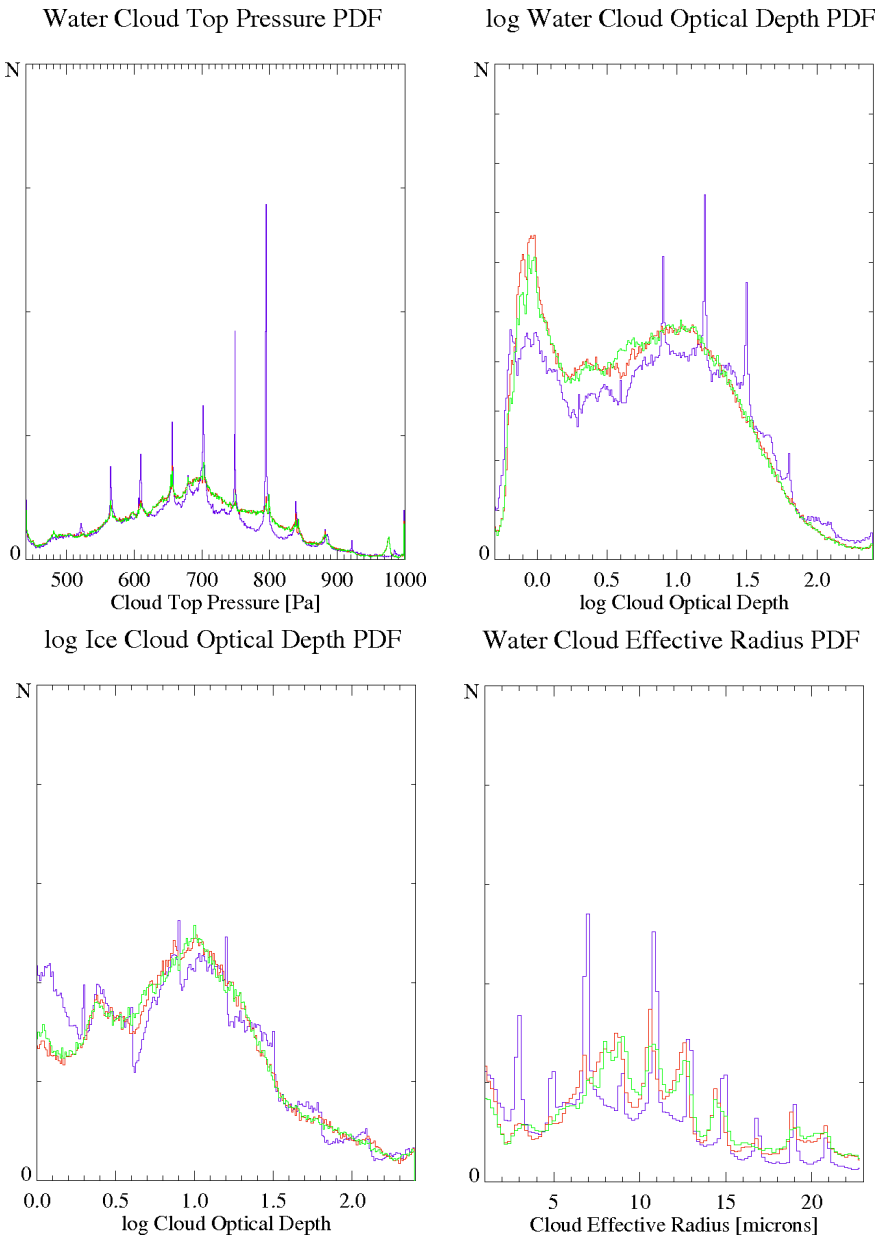

Figure 23: Histograms of the water cloud top pressure, water/ice cloud optical depth and water cloud effective radius as retrieved by ORAC-ATSR for four orbits from the 1st January 2001. The blue line represents the original linear interpolation, the red line represents the 'bicubic sceme' and the green line represents the 2D spline interpolation scheme.

The new interpolation schemes do indeed remove the majority of the ‘spikes’ in the retrieved data, although a small number of features persist. There is some evidence that these features occur where there is a steep forward model gradient, but further investigation is underway to establish the exact cause of *all* of the retrieval artefacts.

It is interesting to investigate the effect of the interpolation schemes on the retrieved products on a pixel by pixel basis. It is not expected that the use of a different interpolation scheme would change the retrieved value of a parameter by more than twice the spacing of the LUT points in that parameter. We would not, for example expect a change in effective radius of more than 4 μm in any pixel.

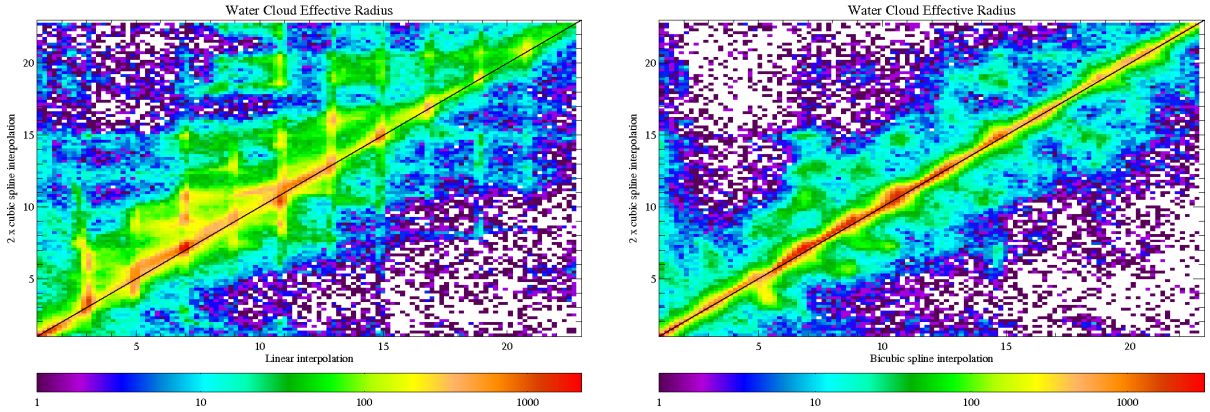

(a) Linear and 2×spline interpolation (b) Bicubic and 2×spline interpolation

Figure 24: A comparison of ORAC-ATSR effective radius retrievals when different interpolation schemes are implemented in the FM.

A comparison between the effective radius retrieved when the linear and 2D spline interpolation methods are used is given in figure 24(a). Although the majority of points lie within 4 μm of the $y = x$ line, a significant number of points lie outside this range. Although the scatter observed in the other parameters tends to be much smaller, this scatter indicates that the interpolation method used can have a profound impact on the retrieval. Figure 24(b) shows the same comparison between the bicubic spline and the 2D spline interpolation methods. Again, a great deal of scatter is observed, although a higher fraction of the points do lie within 4 μm of each other.

The clear impact of the interpolation scheme used in the retrieval on the retrieved parameters indicates that a great deal of analysis is required before a new interpolation scheme is implemented operationally. The interpolation schemes have been tested extensively to check for any errors in the code and a model to establish the exact cause of the ‘spikes’ in the retrieved parameters is under development. Although there is compelling empirical evidence for the implementation of a higher

order interpolation scheme, further work is needed to establish the best scheme to use.

The study on LUT/RTM interpolation has not yet been completed, but a number of improvements to be applied to the ORAC-ATSR interpolation schemes have already been identified and are discussed briefly below.

- **Look up table format.** At present, the ORAC LUTs are stored as ASCII files. When the LUT values are imported into the retrieval they are treated as 'floating point numbers' by the FORTRAN code. The difference in precision between these data formats can result in 'noise' being added to the data. Although this is unlikely to have a significant effect on the interpolated values, it can have a significant effect on the gradient estimates where there is a low information content in the LUT (the LUT gradient is ≈ 0). When a spline interpolation is employed in the retrieval, small changes in the LUT values can cause the splines to 'oscillate'; there is some evidence of this behaviour in the gradient of the diffuse transmission in the 0.67 μm channel with respect to effective radius, as shown in figure 22. In future, the LUTs used in the ORAC-ATSR retrieval will be stored in a binary format to eliminate 'noise' in the data.

- **Spacing of LUT points.** Currently, points in the LUTs of cloud radiative properties are distributed evenly in parameter space. In order to achieve a better interpolation, it is more appropriate to distribute the LUT points according to the gradient with respect to each parameter. Thus, a large number of LUT points should be placed where the gradient is steep and very few where the gradient is shallow. This would increase the accuracy of the interpolation and reduce the potential for 'oscillations' to occur if a cubic spline interpolation were implemented in the scheme. The ORAC-ATSR interpolation scheme has already been generalised to allow non-uniform spacing of LUT points and to allow different LUT point spacing in each LUT.

- **Phase transitions in the ORAC-ATSR retrieval.** At present, phase transitions in the ORAC-ATSR retrieval are driven by the retrieved effective radius. In future versions of ATSR, a retrieval will be performed for both ice and water cloud and the best fit selected using the quality control parameters; this approach may allow some identification of mixed phase clouds.

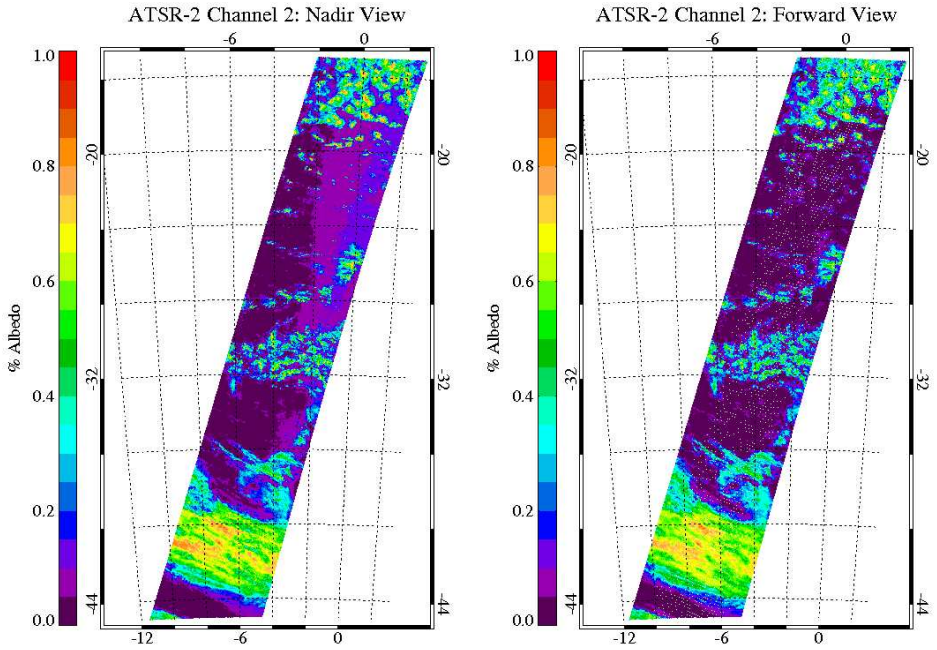

Figure 25: Sun normalised reflectance measurements in the 0.67 μm channel: forward and nadir view.

5.2 Developing the forward-view retrieval

The most recent version of the ORAC-ATSR cloud retrieval data was generated using only nadir-view measurements from the ATSR-2 instrument. During the past year, the retrieval code has been developed to perform retrievals using measurements from **either** the nadir **or** the forward view. A scene over the southern Atlantic Ocean has been chosen to compare the nadir and forward view retrievals. The scene was observed by ATSR-2 on the morning of the 1st January 2001.

Figure 25 shows the sun-normalised reflectance measured at 0.67 μm for both viewing geometries. The effects of sun-glint are clearly visible in the nadir view data, but elsewhere the measurements in the two views are highly correlated.

Figure 26 shows the brightness temperature measurements made in the 11μm and 12μm channels for both views. There is a very high correlation between the measurements in the 11 μm channels, but a greater brightness temperature difference between the 11μm and 12μm channels is observed in the forward view measurements. A large brightness temperature difference between the 11μm and 12μm channels is a well-known indicator of thin cirrus clouds. Clouds have a greater transmission in the 11μm channel than the 12μm channel and so the 11μm tends to ‘see’ deeper into any cloud than the 12μm channel. When thin cirrus is present, it dominates the signal in the 12μm channel while

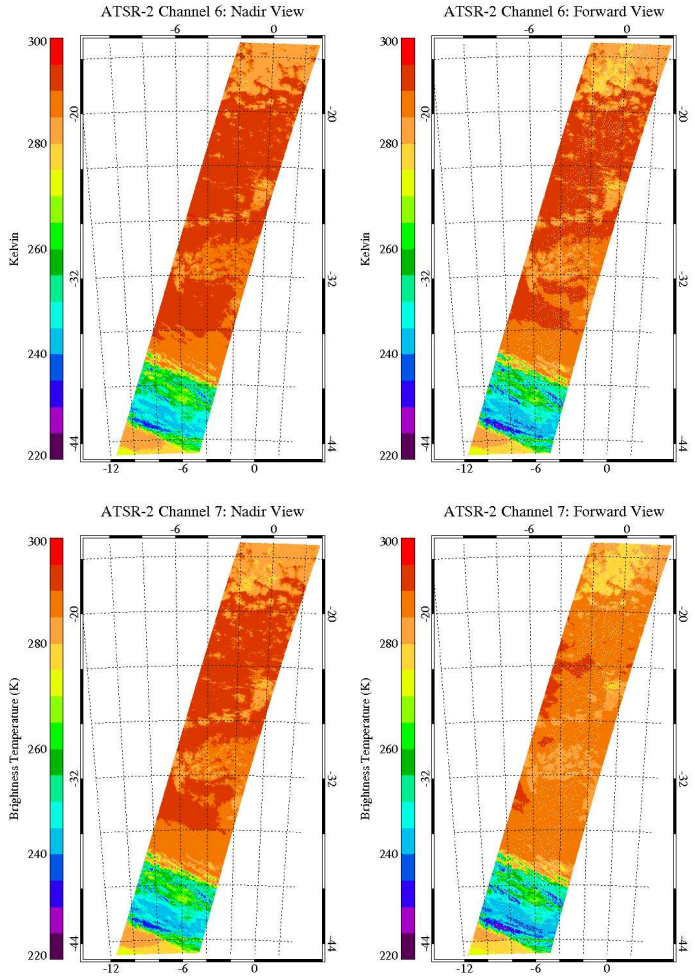

Figure 26: Brightness temperature measurements in the 11 μm (Channel 6) and 12 μm (Channel 7) channels: forward view and nadir view.

the 11μm receives significant contributions from the atmosphere below the cloud, resulting in a large brightness temperature difference between the channels.

5.2.1 A note on parallax

It is important to note the effect of parallax on the ATSR-2 cloud measurements. The latitude and longitude values assigned to each ATSR-2 measurement pixel are based on the ground location that the instrument would observe under *'clear sky'* conditions. If the scene is cloudy however, this will not correspond to the actual location of the cloud over the Earth's surface, as shown in figure 27(a).

It is straightforward to correct for the parallax using the cloud top height, the instrument zenith angle θ_{v}, (which gives the magnitude of the correction) and the instrument azimuth angle ϕ_{v}, (which gives the direction of the correction as shown in figure 27(b)). At present, the instrument azimuth

angle ϕ_v is not part of the ORAC-ATSR output however and so this correction cannot be applied.

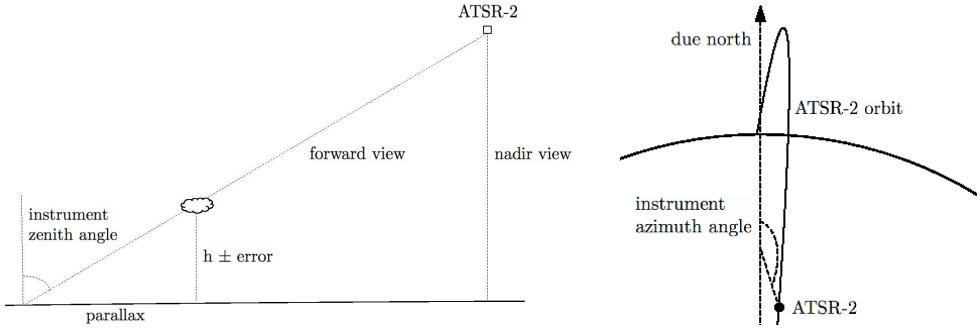

(a) Parallax in the ATSR-2 cloud measurements (b) The instrument azimuth angle

Figure 27: The implications of the ATSR viewing geometry for the collocation of cloud retrievals using the nadir and forward view radiance measurements.

An indication of the effect of the parallax difference between the two views is given by the magnitude of the correction applied at the Earth's surface. The forward view has a typical instrument zenith angle of $\sim 55°$ and so the magnitude of the parallax correction at the surface is a factor of ~ 1.4 times the cloud top height. It is clear that the effect of parallax is likely to account for a large proportion of the scatter in any comparison between forward and nadir view retrievals. Until parallax is accounted for, it is not possible to use any straightforward statistical methods to compare the forward and nadir view retrievals.

5.2.2 Comparison of retrieved parameters

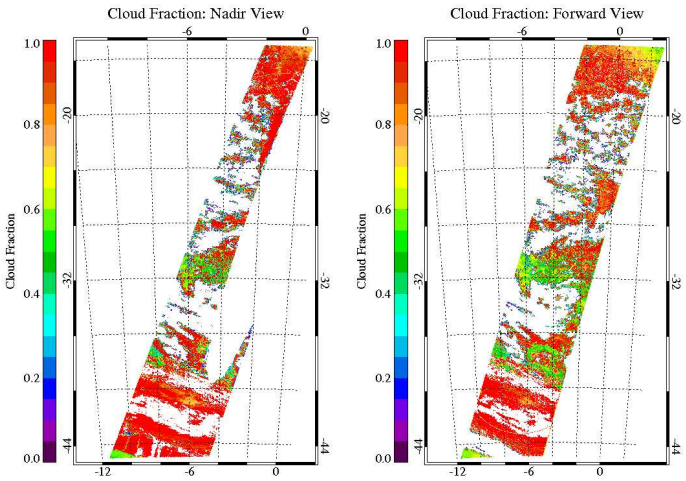

Figure 28: The cloud fraction retrieved by ORAC-ATSR using the nadir and forward view measurements respectively. Retrievals are not performed in the sun-glint region of the nadir view.

Figure 28 shows the cloud fraction retrieved using the forward and nadir view radiances respectively. No retrieval is performed in the sun-glint region of the nadir scene. In general the two images are highly correlated, but there appears to be an anomalous region of high cloud fraction at a latitude of $\sim$ -44° in the nadir view. The origin of this anomalous region is not clear, since no great discrepancy between the forward and nadir view is visible in any of the 'raw' radiance data for this region.

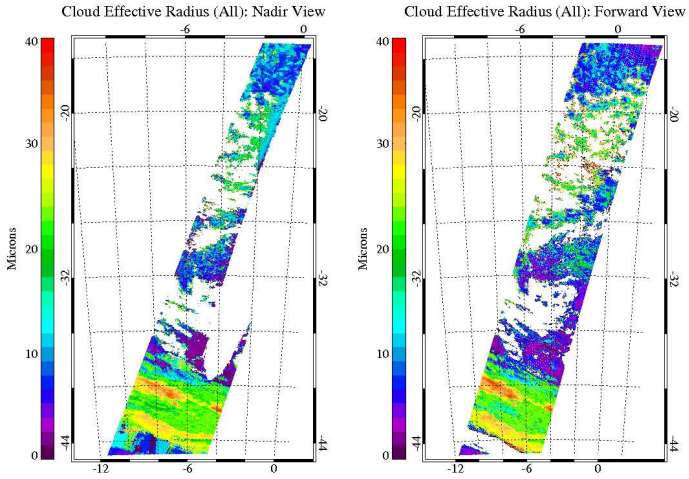

Figure 29: The cloud effective radius retrieved by ORAC-ATSR using the nadir and forward view measurements respectively. Retrievals are not performed in the sun-glint region of the nadir view.

In figure 29 retrievals of cloud effective radius using data from the nadir and forward views are compared. Again, the two views appear to produce highly consistent retrievals, apart from the narrow 'band' of anomalous data in the nadir view at $\sim$ -44°. Between the latitudes of $\sim$ -20° and -28°, there are patchy regions of cloud and 'edge effects' are visible, particularly in the forward view retrieved data. This is likely to be the result of the increased level of horizontal inhomogeneity towards the cloud edge and the different locations of cloud shadows in the forward and nadir views.

Figure 30 shows histograms of cloud top pressure from 15 orbits from October 2000, as retrieved using the nadir and the forward view radiance measurements respectively. The histograms have been normalised to allow a comparison between the two views and an arbitrary linear scale is used for the y axis. In both cases only retrievals with a cost < 30 that converged in fewer than 8 iterations have been included. It is clear that a greater proportion of high cloud and optically thin cloud is retrieved using the forward view. This is consistent with expectations, due to the longer atmospheric path length of the forward view.

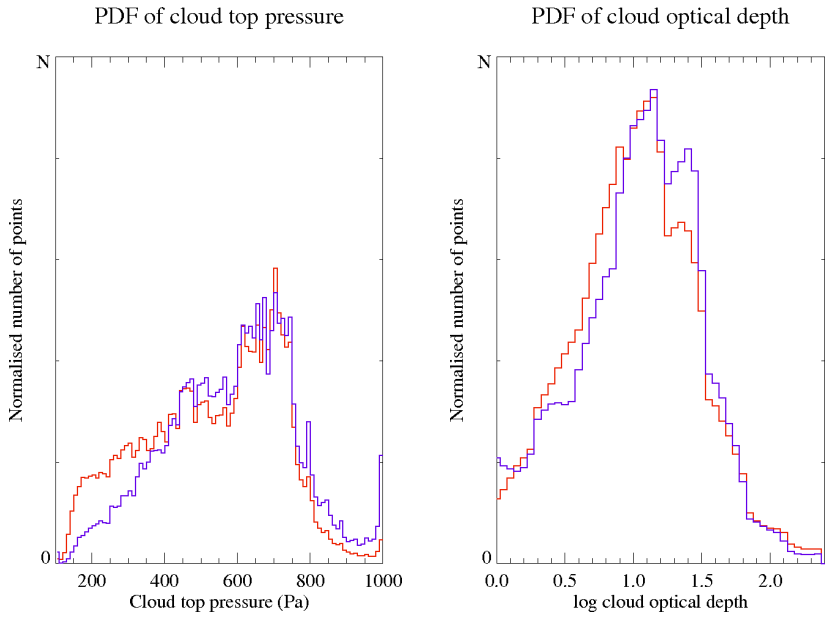

Figure 30: Histograms of retrieved cloud top pressure and cloud optical depth. The values retrieved using the nadir view measurements correspond to the blue line and the red line corresponds to the values retrieved using the forward view.

5.3 Towards a dual-view cloud retrieval

5.3.1 Why use both views?

The use of both the forward and the nadir measurements from ATSR in the ORAC retrieval scheme has a number of potential advantages. First of all, the amount of information 'ingested' by the retrieval is effectively doubled, which should improve coverage and reduce the standard errors in the retrieved parameters. The addition of the forward view does more than just increase the quantity of data however: the different viewing geometries have different sensitivities to the cloud effective radius, because the phase functions of ice crystals and water droplets are dependent on the viewing geometry. The forward view provides more information on thin, high clouds, but the nadir view is less prone to the effects caused by cloud shadows or cloud inhomogeneity. Using data from both views there is potential to retrieve in the sun-glint region and to resolve multilayer cloud systems under some conditions.

5.3.2 Potential approaches.

There are two potential approaches for a dual-view cloud retrieval scheme for ATSR-2. These approaches are outlined below and their potential strengths and weaknesses are identified.

Sequential estimation

The sequential estimation approach involves using a retrieval performed using the measurements from one view to set the *a priori* information for a second retrieval, using the measurements from the other view. This technique requires the development of a very rigorous error budget: with both *a priori* information and measurements playing a significant role in the retrieval, it is very important to ensure that errors are characterised correctly; this method then allows the full power of optimal estimation to be exploited. An advantage of sequential estimation is the potential to use the first retrieval to identify 'difficult' scenes in the second retrieval.

Increasing the measurement vector

An alternative approach to sequential estimation is to extend the measurement vector to include both the nadir and the forward view radiances. A clear difficultly with this approach is the parallax between the two views, as described in section 5.2.1; it is not possible to properly collocate the nadir and forward view measurements until a cloud top height retrieval has been undertaken. With a greater number of measurements to fit, this method could result in the convergence of a smaller number of retrievals. This method is however likely to be more computationally efficient than a sequential estimation approach.

5.4 Identifying poorly modelled scenes

The principal source of error in the ORAC-ATSR retrieval identified in the previous chapter is the poor characterisation of certain scenes. The ORAC-ATSR FM provides a poor representation of three major scene types: multi-layered cloud, snow-covered (and mountainous) regions and ocean regions containing a significant quantity of sea ice. In order to improve the retrieval performance over these scenes it is first necessary to develop an accurate means of identifying them. Sea ice, snow cover and multilayer cloud masks have all been developed for the AVHRR and MODIS instruments [Hall et al., 1998; Wind et al., 2009; Minnis et al., 2005; Gesell, 1989; Heidinger and Pavolonis, 2005]: given the similarity of the ATSR-2 and AVHRR channels (and to a lesser extent the MODIS channels) it should be possible to design similar masks for ATSR-2.

Once 'difficult' scenes have been identified, fairly simple alterations can be made to the forward

model in order to better represent the scene. Sea-ice, for example can be easily characterised by an adjustment of the FM surface reflectance. Finding methods for detecting ‘difficult’ scenes is an active area of development in the ORAC-ATSR retrieval. There is significant evidence that there is sensitivity in the ATSR-2 measurement to such scenes, but any new ‘mask’ must be validated extensively before it is incorporated into the operational retrieval.

References

Ackerman et al., A. [2000], 'Reduction of tropical cloudiness by soot', *Science* **288**(5468), 1042–1047.

Aminou, D. M. A. [2002], 'MSG's SEVIRI Instrument', *ESA Bulletin* (111), 15–17.

Barkstrom, B. R., Harrison, E. F. and Lee, III, R. B. [1990], 'Earth Radiation Budget Experiment - Preliminary seasonal results', *EOS Transactions* **71**, 279+.

Bovensmann, H., Burrows, J. P., Buchwitz, M., Frerick, J., Noël, S., Rozanov, V. V., Chance, K. V. and Goede, A. P. H. [1999], 'SCIAMACHY: Mission Objectives and Measurement Modes', *Journal of Atmospheric Sciences* **56**, 127–150.

Bréon, F.-M., Tanré, D. and S.Generoso [2002], 'Aerosol effect on cloud droplet size monitored from satellite', *Science* **295**(834), 834–838.

Brown, J., Hoke, M., Doherty, K., Anderson, G. and Berk, A. [2004], *MODTRAN 4 Software*. http://www.vs.afrl.af.mil/ProductLines/IR-Clutter/modtran4.aspx [Accessed 7 August 2009].

Bulgin, C. E., Palmer, P. I., Thomas, G. E., Arnold, C. P. G., Campmany, E., Carboni, E., Grainger, R. G., Poulsen, C., Siddans, R. and Lawrence, B. N. [2008], 'Regional and seasonal variations of the Twomey indirect effect as observed by the ATSR-2 satellite instrument', *Geophysical Research Letters* **35**, 2811+.

Burrows, J. P., Holzle, E., Goede, A. P. H., Visser, H. and Fricke, W. [1995], 'Sciamachy–Scanning imaging absorption spectrometer for atmospheric chartography', *Acta Astronautica* **35**, 445–451.

Campmany, E., Grainger, R. G., Dean, S. and Sayer, A. M. [2009], 'Automatic detection of ship-tracks in ATSR-2 satellite imagery', *Atmospheric Chemistry and Physics* **9**, 1899–1905.

Cox, C. S. and Munk, W. H. [1954*a*], 'Measurement of the roughness of the sea surface from photographs of the Sun's glitter', *J. Opt. Soc. Am.* **44**, 838–850.

Cox, C. S. and Munk, W. H. [1954*b*], 'Statistics of the sea surface derived from Sun glitter', *J. Mar. Res.* **13**, 198–227.

Delderfield, J., Llewellyn-Jones, D. T., Bernard, R., de Javel, Y. and Williamson, E. J. [1986], The Along Track Scanning Radiometer (ATSR) for ERS1, *in* J. S. Seeley, J. W. Lear, S. L. Russak and A. Monfils, eds, 'Society of Photo-optical Instrumentation Engineers (SPIE) Conference Series', Vol. 589, pp. 114–120.

Denis, M. A., Muller, J. P. and Mannstein, H. [2007], 'ATSR-2 camera models for the automated stereo photogrammetric retrieval of cloud-top heights-initial assessments', *Int. J. Remote Sens.* **28**(9), 1939–1955.

Diner, D. J., Beckert, J. C., Reilly, T. H., Bruegge, C. J., Conel, J. E., Kahn, R. A., Martonchik, J. V., Ackerman, T. P., Davies, R., Gerstl, S. A. W., Gordon, H. R., Muller, J., Myneni, R. B., Sellers, P. J., Pinty, B. and Verstraete, M. M. [1998], 'Multi-angle Imaging SpectroRadiometer (MISR) instrument description and experiment overview', *IEEE Transactions on Geoscience and Remote Sensing* **36**, 1072–1087.

Doelling, D. R., Nguyen, L. and Minnis, P. [2004], On the use of deep convective clouds to calibrate AVHRR data, *in* Barnes, W. L. and Butler, J. J., ed., 'Society of Photo-Optical Instrumentation Engineers (SPIE) Conference Series', Vol. 5542, pp. 281–289.

ECMWF [2006], *European Centre for Medium-Range Weather Forecasts Home Page*. http://www.ecmwf.int/ [Accessed 11 August 2009].

Edwards, T., Browing, R., Delderfield, J., Lee, D. J. and A., L. K. [1990], 'The along track scanning radiometer - Measurement of sea-surface temperature from ERS-1', *Journal of the British Interplanetary Society* **43**, 160–180.

Evan, A. T., Heidinger, A. K. and Vimont, D. J. [2007], 'Arguments against a physical long-term trend in global ISCCP cloud amounts', *Geophysical Research Letters* **34**, 4701+.

Fischer, H., Birk, M., Blom, C., Carli, B., Carlotti, M., von Clarmann, T., Delbouille, L., Dudhia, A., Ehhalt, D., Endemann, M., Flaud, J. M., Gessner, R., Kleinert, A., Koopmann, R., Langen, J., López-Puertas, M., Mosner, P., Nett, H., Oelhaf, H., Perron, G., Remedios, J., Ridolfi, M., Stiller, G. and Zander, R. [2007], 'MIPAS: an instrument for atmospheric and climate research', *Atmospheric Chemistry & Physics Discussions* **7**, 8795–8893.

Francis, C. R., Graf, G., Edwards, P. G., McCraig, M., McCarthy, C., Lefebvre, A., Pieper, B., Pouvreau, P. Y., Wall, R. and Weschler, F. [1995], 'The ERS-2 spacecraft and its payload', *ESA Bulletin* (83), 13–31.

Gesell, G. [1989], 'An algorithm for snow and ice detection using AVHRR data An extension to the APOLLO software package', *International Journal of Remote Sensing* **10**, 897–905.

Goddard, J. [1995], 'The Chilbolton radar facility', *IEE Seminar Digests* **1995**(34), 6.

González, A., Wendling, P., Mayer, B., Gayet, J.-F. and Rother, T. [2002], 'Remote sensing of cirrus cloud properties in the presence of lower clouds: An ATSR-2 case study during the Interhemispheric Differences in Cirrus Properties From Anthropogenic Emissions (INCA) experiment', *Journal of Geophysical Research (Atmospheres)* **107**, 4693+.

Hall, D. K., Riggs, G. A. and Salomonson, V. V. [1998], *Algorithm Theoritical Basis Document (ATBD) for the MODIS snow and sea-ice mapping algorithms*. http://modis-snow-ice.gsfc.nasa.gov/atbd.html [Accessed 7 August 2009].

Heidinger, A. K. and Pavolonis, M. J. [2005], 'Global Daytime Distribution of Overlapping Cirrus Cloud from NOAA's Advanced Very High Resolution Radiometer.', *Journal of Climate* **18**, 4772–4784.

Hurley, J., Dudhia, A. and Grainger, R. G. [2009], 'Cloud detection for MIPAS using singular vector decomposition', *Atmospheric Measurement Techniques Discussions* **2**(2), 1185–1219.
URL: *http://www.atmos-meas-tech-discuss.net/2/1185/2009/*

Ignatov, A., Cao, C., Sullivan, J., Kihai, Y., Heidinger, A., Jelenak, A., Jarva, K., Goodrum, G., Galvin, R., Tarpley, D., Goldberg, M., Bates, J. and Bayler, E. [2005], 'Towards long-term characterization of AVHRR sensors for the NOAA/NESDSIS science data stewardship program: Focus on NOAA-16 and NOAA-17 in 2003', *Geophysical Research Abstracts* **7**(09515), 1–2.

Intergovernmental Panel on Climate Change [2007], 'Climate Change 2007: The Physical Science Basis - Summary for Policymakers', www.ipcc.ch/SPM2feb07.pdf.

Jacobowitz, H., Stowe, L. L., Ohring, G., Heidinger, A., Knapp, K. and Nalli, N. R. [2003], 'The Advanced Very High Resolution Radiometer Pathfinder Atmosphere (PATMOS) Climate Dataset: A Resource for Climate Research.', *Bulletin of the American Meteorological Society* **84**, 785–793.

Kidwell, K. B. [2009], *NOAA KLM user's guide*, February 2009 revised edn. http://www.ncdc.noaa.gov/oa/pod-guide/ncdc/docs/klm/index.htm [Accessed 15th August 2009].

Köhler, H. [1936], 'The Nucleus in and the growth of hygroscopic droplets', *Trans. Faraday. Soc.* **32**, 1152–1161.

Kokhanovsky, A. A., Rozanov, V. V., Burrows, J. P., Eichmann, K.-U., Lotz, W. and Vountas, M. [2005], 'The SCIAMACHY cloud products: Algorithms and examples from ENVISAT', *Advances in Space Research* **36**, 789–799.

Koren, I., Kaufman, Y. J., Rosenfeld, D., Remer, L. A. and Rudich, Y. [2005], 'Aerosol invigoration and restructuring of Atlantic convective clouds', *Geophysical Research Letters* **32**, 14828.

Levenburg, K. [1944], 'A method for the solution of certain nonlinear problems in least squares', *Quarterly Journal of Applied Mathematics* **2**, 164–168.

Llewllyn-Jones, D., Edwards, M. C., Mutlow, C. T., Birks, A. R., Barton, I. J. and Tait, H. [2001], 'AATSR: Global-Change and Surface-Temperature Measurements from Envisat', *ESA Bulletin* (105), 11–21.

Lohmann, U. and Feichter, J. [2005], 'Global indirect aerosol effects: a review', *Atmospheric Chemistry & Physics* **5**, 715–737.

Louet, J. [2001], 'The Envisat Mission and System', *ESA Bulletin* (106), 10–25.

Macke, A., Mishchenko, M. I., Muinonen, K. and Carlson, B. E. [1995], 'Scattering of light by large nonspherical particles: ray-tracing approximation versus T-matrix method', *Optics Letters* **20**, 1934–1936.

Marquardt, D. W. [1963], 'An Algorithm for Least-Squares Estimation of Nonlinear Parameters', *SIAM Journal on Applied Mathematics* **11**(2), 431–441.

Mason, I. M., Sheather, P. H., Bowles, J. A. and Davies, G. [1996], 'Blackbody calibration sources of high accuracy for a spaceborne infrared instrument: the Along Track Scanning Radiometer', *Applied Optics* **35**(4), 629–639.

Mie, G. [1908], 'Pioneering mathematical description of scattering by spheres', *Ann. Phys.* **25**, 337.

Minnis, P., Sun-Mack, S., Chen, Y., Yi, H., Huang, J., Nguyen, L. and Khaiyer, M. M. [2005], Detection and retrieval of multi-layered cloud properties using satellite data, *in* K. Schäfer, A. T. Comerón, J. R. Slusser, R. H. Picard, M. R. Carleer and N. Sifakis, eds, 'Society of Photo-Optical Instrumentation Engineers (SPIE) Conference Series', Vol. 5979, pp. 70–78.

Minnis, P., Young, D. F., Wielicki, B. A., Sun-Mack, S., Trepte, Q. Z., Chen, Y., Heck, P. W. and Dong, X. [2003], A global cloud database from VIRS and MODIS for CERES, *in* H.-L. Huang, D. Lu and Y. Sasano, eds, 'Society of Photo-Optical Instrumentation Engineers (SPIE) Conference Series', Vol. 4891, pp. 115–126.

Moroney, C., Davies, R. and Muller, J.-P. [2002], 'Operational retrieval of cloud-top heights using MISR data', *IEEE Transactions on Geoscience and Remote Sensing* **40**, 1532–1540.

Muller, J. P., Denis, M. A., Dundas, R. D., Mitchell, K. L., Naud, C. and Mannstein, H. [2007], 'Stereo cloud-top heights and cloud fraction retrieval from ATSR-2', *Int. J. Remote Sens.* **28**(9), 1921–1938.

Mutlow, C. T., Murray, J., Bailey, P., Birks, A. and Smith, D. [1999], *ATSR-1/2 User Guide*, 1st edn, ESA. http://earth.esa.int/ers/atsr/ [Accessed 29 July 2009].

Mutlow, C. T., Smith, D. L. and Murray, M. J. [2000], 'The Along Track Scanning Radiometer (ATSR) Instruments on ERS-1 and ERS-2', *Earth Observation Quarterly* (65), 1–5.

Naud, C., Mitchell, K. L., Muller, J.-P., Clothiaux, E. E., Albert, P., Preusker, R., Fischer, J. and Hogan, R. J. [2007], 'Comparison between ATSR-2 stereo, MOS O2-A band and ground-based cloud top heights', *International Journal of Remote Sensing* **28**, 1969–1987.

Nieke, J., Frerick, J., Stroede, C., Mavrocordatos, C. and Berruti, B. [2008], 'Status of the optical payload and processor development of ESA's Sentinel-3 mission', Abstract for IEEE International Geoscience and Remote Sensing Symposium, Boston, Massachusetts, U.S.A., Jul 6–11, 2008.

North, P., Brockmann, C., Fischer, J., Gomez-Chova, L., Grey, W., Moreno, J., Preusker, R. and Regner, P. [2008], MERIS/AATSR Synergy Algorithms for Cloud Screening, Aerosol Retrieval and Atmospheric Correction, *in* '2nd AATSR and MERIS User Workshop', ESRIN, Frascati, Italy. http://earth.esa.int/workshops/meris_aatsr2008/participants/434/pres_434_North.pdf [Accessed 17 Aug 2009].

Olesen, F. [2005], *DISORT Algorithm*. http://imk-msa.fzk.de/msa-public/Software-tools/Modtran/science/disort.htm [Accessed 7 August 2009].

Platnick, S., King, M. D., Ackerman, S. A., Menzel, W. P., Baum, B. A., Riedi, J. C. and Frey, R. A. [2003], 'The MODIS cloud products: algorithms and examples from terra', *IEEE Transactions on Geoscience and Remote Sensing* **41**, 459–473.

Poulsen, C. A., Siddans, R., Lawrence, B., Sayer, A., Thomas, G., Grainger, R. G., Dean, S. and Arnold, C. [2009], 'Cloud retrievals from satellite data using Optimal Estimation and Application to ATSR', *Remote Sensing of the Environment* . In preparation.

Press, W. H., Flannery, B. P., Teukolsky, S. A. and Vetterling, W. [1987], *Numerical recipes: the art of scientific computing*, Cambridge University Press.

Press, W. H., Flannery, B. P., Teukolsky, S. A. and Vetterling, W. [1996], *Numerical recipes in Fortran 90: the art of* parallel *scientific computing*, Cambridge University Press.

Quaas, J., Boucher, O., Bellouin, N. and Kinne, S. [2008], 'Satellite-based estimate of the direct and indirect aerosol climate forcing', *Journal of Geophysical Research (Atmospheres)* **113**, 5204+.

Rao, C. R. N. and Chen, J. [1996], 'Post-launch calibration of the visible and near-infrared channels of the Advanced Very High Resolution Radiometer on the NOAA-14 spacecraft', *International Journal of Remote Sensing* **17**, 2743–2747.

Rodgers, C. [2000*a*], *An introduction to inverse methods in remote sounding*, World Scientific Press, Singapore.

Rodgers, C. [2000*b*], *Inverse methods for atmospheric sounding: Theory and Practice*, Series on Atmospheric, Oceanic and Planetary Physics–Vol. 2, World Scientific Press.

Roebeling, R. A., Hauschildt, H., Jolivet, D., Meijgaard, E. and J.Feijt, A. [2003], Retrieval and validation of MSG and AVHRR based cloud physical parameters in the CMSAF, *in* 'Proceedings of the EUMETSAT data users conference', EUMETSAT, pp. 183–198.

Rosenfeld, D. [1999], 'TRMM observed first direct evidence of smoke from forest fires inhibiting rainfall', *Geophysical Research Letters* **26**(20), 3105–3108.

Rosenfeld, D. [2000], 'Suppression of rain and snow by urban and industrial air pollution', *Science* **287**(5459), 1793–1796.

Rossow, W. B. and Schiffer, R. A. [1991], 'ISCCP Cloud Data Products.', *Bulletin of the American Meteorological Society* **72**, 2–20.

Rossow, W. B. and Schiffer, R. A. [1999], 'Advances in Understanding Clouds from ISCCP', *Bulletin of the American Meteorological Society* **80**, 2261–2288.

Rozanov, V., Kokhanovsky, A., Loyola, D., Siddans, R., Latter, B., Stevens, A. and Burrows, J. [2006], 'Intercomparison of cloud top altitudes as derived using gome and atsr-2 instruments on-board ers-2', *Remote Sensing of Environment* **102**, 186–193.

Salomonson, V. V., Barnes, W. L., Maymon, P. W., Montgomery, H. E. and Ostrow, H. [1989], 'MODIS: advanced facility instrument for studies of the Earth as a system', *IEEE Transactions on Geoscience and Remote Sensing* **27**(2), 145–153.

Salomonson, V. V., Barnes, W., Xiong, J., Kempler, S. and Masuoka, E. [2002], An overview of the Earth Observing System MODIS instrument and associated data systems performance, *in* 'Geoscience and Remote Sensing Symposium, 2002. IGARSS '02. 2002 IEEE International', Vol. 2, pp. 1174–1176.

Saunders, R., English, s., Rayer, P., Matricardi, M., Chevallier, F., Brunel, P. and DeBlonde, G. [2002], *RTTOV-7: A Satellite Radiance Simulator for the New Millenium*.
http://cimss.ssec.wisc.edu/itwg/itsc/itsc12/rws_lorne.pdf
[Accessed 13 August 2009].

Saunders, R., Matricardi, M. and Brunel, P. [1999], 'An improved fast radiative transfer model for assimilation of satellite radiance observations', *Quarterly Journal of the Royal Meteorological Society* **125**, 1407–1425.

Scatterfield, L., O'Bannon, J. and Vermote, E. F. [2004], *MODIS Land Surface Reflectance Home Page*.
http://modis-land.gsfc.nasa.gov/ [Accessed 11 August 2009].

Sidran, M. [1981], 'Broadband reflectance and emissivity of specular and rough water surfaces', *Appl. Opt.* **20**(18), 3176–3183.

Smith, D. L. [1997], Calibration of the ATSR-2 visible channels using deep convection clouds and desert scenes, *in* 'Proceedings of the 3rd ERS-1 Symposium, Space at the Service of Our Environment', Florence, Italy.

Smith, D. L. [2008], ATSR-2 and AATSR performance, *in* '2nd AATSR and MERIS User Workshop', ESRIN, Frascati, Italy.
http://earth.esa.int/workshops/meris_aatsr2008/participants/493/pres_493_ Smith.pdf
[Accessed 17 Aug 2009].

Smith, D. L., Mutlow, C. T. and Rao, C. R. N. [2002], 'Calibration monitoring of the visible and near-infrared channels of the Along-Track Scanning Radiometer-2 by use of stable terrestrial sites', *Applied Optics* **41**(3), 515–523.

Smith, D. L., Read, P. D. and Mutlow, C. T. [1997], 'Calibration of the visible/near-infrared channels of the Along-Track Scanning Radiometer-2 (ATSR-2)', *Sensors, Systems, and Next-Generation Satellites* **3221**(1), 53–62.

Solomon, S., Qin, D., Manning, M., Chen, Z., Marquis, M., Averyt, K. B., Tignor, M. and Miller, H. L., eds [2007], *Climate Change 2007: The Physical Science Basis. Contribution of Working Group I to the Fourth Assessment Report of the Intergovernmental Panel on Climate Change*, Cambridge University Press, Cambridge, United Kingdom and New York, NY, USA.

Stamnes, K., Tsay, S., Wiscombe, W. and Jayaweera, K. [1988], 'Numerically stable algorithm for discrete ordinate method radiative transfer in multiple scattering and emitting layered media', *Appl. Opt.* **27**(12), 2502–2509.

Stephens, G. L., Vane, D. G., Boain, R. J., Mace, G. G., Sassen, K., Wang, Z., Illingworth, A. J., O'Connor, E. J., Rossow, W. B., Durden, S. L., Miller, S. D., Austin, R. T., Benedetti, A., Mitrescu, C. and The Cloudsat Science Team [2002], 'The Cloudsat Mission and the A-Train', *Bulletin of the American Meteorological Society* **83**, 1771–1790.

Stokes, G. M. and Schwartz, S. E. [1994], 'The Atmospheric Radiation Measurement (ARM) Program: Programmatic Background and Design of the Cloud and Radiation Test Bed.', *Bulletin of the American Meteorological Society* **75**, 1201–1222.

Stowe, L. L., Jacobowitz, H., Ohring, G., Knapp, K. R. and Nalli, N. R. [2002], 'The Advanced Very High Resolution Radiometer (AVHRR) Pathfinder Atmosphere (PATMOS) Climate Dataset: Initial Analyses and Evaluations', *Journal of Climate* **15**, 1243–1260.

Stubenrauch, C., Kinne, S. and The GEWEX Cloud Assessment Team [2009], 'Assessment of global cloud climatologies', *GEWEX News* **19**(1), 6–7.

Takano, Y. and Liou, K. [1989], 'Solar Radiative Transfer in Cirrus Clouds. Part I: Single-Scattering and Optical Properties of Hexagonal Ice Crystals.', *J. Atmos. Sci.* (46), 3–19.

Thomas, G. E., Poulsen, C. A., Sayer, A. M. Siddans, R., Lawrence, B., Campmany, E., Grainger, R. G., Dean, S. and Watts, P. D. [2009], 'Validation of GRAPE aerosol data'. In preparation.

Thoss, A. [2008], 'Report on the Cloud Parameter Retrieval Workshop, 17–19 May 2006 Norrköping', http://nwcsaf.inm.es/VSA/cws_2006_report_part1.pdf.

Twomey, S. [1997], 'The influence of pollution on the shortwave albedo of clouds', *Journal of the Atmospheric Sciences* **34**(7), 1149–1152.

Wanner, W., Strahler, A. H., Hu, B., Lewis, P., Muller, J. P., Li, X., Schaaf, C. L. B. and Barnsley, M. J. [1997], 'Global retrieval of bidirectional reflectance and albedo over land from EOS MODIS and MISR data: Theory and algorithm', *J. Geophys. Res.* **102**, 17143–17161.

Warren, S. G. [1984], 'Optical constants of ice from the ultraviolet to the microwave', *Appl. Opt.* **23**(8), 1206–1225.

Watts, P. D. [2000], 'MSG SEVIRI Enhanced Cloud Processor Algorithm Theoretical Basis Document', Council for the Central Laboratory of the Research Councils.

Watts, P. D., Mutlow, C. T., Baran, A. J. and Zavody, A. M. [1998], 'Study on cloud properties derived from meteosat second generation observations', *EUMETSAT ITT* (97/181).

Wielicki, B. A., Barkstrom, B. R., Harrison, E. F., Lee, III, R. B., Smith, G. L. and Cooper, J. E. [1996], 'Clouds and the Earth's Radiant Energy System (CERES): An Earth Observing System Experiment.', *Bulletin of the American Meteorological Society* **77**, 853–868.

Wind, G., Platnick, S., King, M., Hubanks, P., Pavolonis, M. J., Heidinger, A., Yang, P. and Baum, B. [2009], 'Multilayer Cloud Detection with the MODIS Near-Infrared Water Vapor Absorption Band', *Journal of Apllied Meterology and Climatology* . In preparation.

Winker, D., Hostetler, C. and Hunt, W. [2004], Caliop: the Calipso LIDAR, *in* Pappalardo, G. and Amodeo, A., ed., '22nd Internation Laser Radar Conference (ILRC 2004)', Vol. 561 of *ESA Special Publication*, pp. 941+.

Winker, D., Vaughan, M. and Hunt, B. [2006], The CALIPSO mission and initial results from CALIOP, *in* 'Society of Photo-Optical Instrumentation Engineers (SPIE) Conference Series', Vol. 6409.

Wiscombe, W. J. [1980], 'Improved Mie scattering algorithms', *Appl. Opt.* **19**(9), 1505–1509.

Woick, H., Dewitte, S., Feijt, A., Gratzki, A., Hechler, P., Hollmann, R., Karlsson, K.-G., Laine, V., Löwe, P., Nitsche, H., Werscheck, M. and Wollenweber, G. [2002], 'The satellite application facility on climate monitoring', *Advances in Space Research* **30**, 2405–2410.

Wrench, C. L. [2009], *Science and Technology Facilities Council (STFC), Chilbolton Facility for Atmospheric and Radio Research (CFARR) data*.
http://badc.nerc.ac.uk/data/chilbolton [Accessed 7 August 2009].

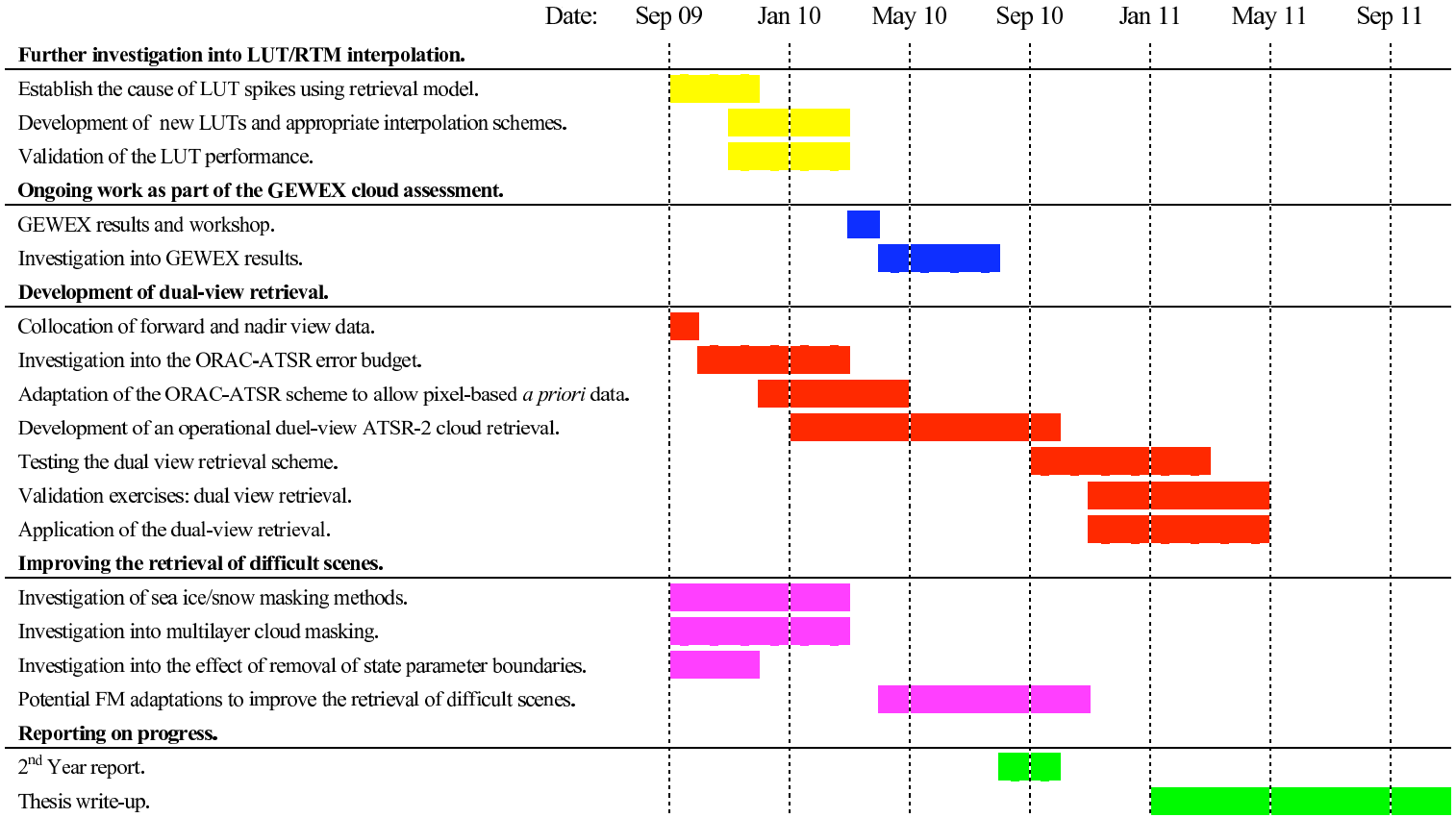
Date:
Sep 09
Jan 10
May 10
Sep 10
Jan 11
May 11
Sep 11
Further investigation into LUT/RTM interpolation.
Establish the cause of LUT spikes using retrieval model.
Development of new LUTs and appropriate interpolation schemes.
Validation of the LUT performance.
Ongoing work as part of the GEWEX cloud assessment.
GEWEX results and workshop.
Investigation into GEWEX results.
Development of dual-view retrieval.
Collocation of forward and nadir view data.
Investigation into the ORAC-ATSR error budget.
Adaptation of the ORAC-ATSR scheme to allow pixel-based a priori data.
Development of an operational duel-view ATSR-2 cloud retrieval.
Testing the dual view retrieval scheme.
Validation exercises: dual view retrieval.
Application of the dual-view retrieval.
Improving the retrieval of difficult scenes.
Investigation of sea ice/snow masking methods.
Investigation into multilayer cloud masking.
Investigation into the effect of removal of state parameter boundaries.
Potential FM adaptations to improve the retrieval of difficult scenes.
Reporting on progress.
2nd Year report.
Thesis write-up.